Structural and Interfacial Characterization of a Sustainable Si/Hard Carbon Composite Anode for Lithium-Ion Batteries

(Article begins on next page)

17 August 2024

Structural and Interfacial Characterization of a Sustainable Si/Hard Carbon Composite Anode for Lithium-ion Batteries

Leonardo Sbrascini,*,† Antunes Staffolani,† Luca Bottoni,† Hamideh Darjazi,† Luca Minnetti,† Marco Minicucci,‡ and Francesco Nobili †,⁑

†School of Science and Technologies – Chemistry Division, University of Camerino, 62032 Camerino, Italy

‡School of Science and Technologies – Physics Division, University of Camerino, 62032 Camerino, Italy

⁑GISEL – Centro di Riferimento Nazionale per i Sistemi di Accumulo Elettrochimico di Energia, INSTM, 50121 Firenze, Italy

*Corresponding author. E-mail: leonardo.sbrascini@unicam.it

ABSTRACT: The effects of a biomass-derived hard carbon matrix and a sustainable crosslinked binder are investigated as electrode components for a silicon-based anode in lithium-ion half-cells, in order to reduce the capacity fade due to volume expansion and shrinkage upon cycling. Ex-situ Raman spectroscopy and impedance spectroscopy are used to deeply investigate the structural and interfacial properties of the material within a single cycle and upon cycling. An effective buffering of the volume changes of the composite electrode is evidenced, even at a high Si content up to 30% in the formulation, resulting in retention of structural and interfacial integrity. As a result, a high capacity performance and a very good rate capability are displayed even at high current densities, with a stable cycling behavior and low polarization effects.

1. INTRODUCTION

The global market has recently started to move from a linear to a perspective of circular economy and environmental sustainability, especially regarding the sector of rechargeable batteries, where implementation in terms of production, recovery and recycling of materials is becoming an extremely important research topic [1–4]. The fast development of Li-ion batteries in recent years and their incredible commercial success led to an increasingly growing market demand, especially due to the ever-rising transport electrification [5,6]. The sector of automotive industry is indeed growing at an increasing rate, focusing on the production of electric vehicles (EVs) in order to lower the environmental impact caused, among other factors, by internal combustion engines [7,8]. Among the others, the low specific capacity of the state-of-the-art graphite anode employed in commercial batteries is becoming a limiting factor in the development of high-energy density devices, thus a progressive substitution of this material at the anode is expected, promoting the use of composite materials that could ensure higher energy densities and specific capacities, with the aim to obtain a suitable driving range per single charge

2

[9,10]. Moreover, in a circular economy perspective, the valorization of waste materials through second-life applications is imperative for reducing the environmental footprint that would otherwise be generated from their immediate disposal [11–13].

For these reasons, researchers have lately moved their attention towards alternative materials that could ensure high performance, while being in line with a low environmental impact. Among these, alloying anodes based on silicon (Si) are the most promising ones because of their high specific capacity at room temperature of 3579 mAh g^{-1} ($Li_{15}Si_4$), low working potential vs. Li^+/Li and relative abundance on Earth's crust, resulting as the best candidates for application in next-generation batteries [14–16]. In spite of its excellent electrochemical characteristics, Si is subjected to huge volume changes upon charge/discharge cycles, which lead to unstable interfaces, electrode pulverization, loss of electrical contact and fast performance decay [17–19]. The use of carbon materials as buffering matrices for the volume expansion of alloying materials is very attractive in order to overcome these issues [20,21]. In particular, the application of Hard Carbons in composite electrodes allows to combine the desirable physical-chemical characteristics of carbon materials, such as good conductivity, porosity and surface area, with the high gravimetric and volumetric energy densities of alloying materials [22,23]. Hard Carbons are also attractive because they can be obtained from waste biomass and, if properly optimized, their synthesis can provide a lower impact with respect to other complex carbon-based matrices such as graphene, both in terms of production cost and energy efficiency [24].

It is also well known that the use of green binders with a high content of polar functional groups such as carboxyl group (-COOH), hydroxyl group (-OH) and amino group ($-NH_2$), can help improving both performance and stability in alloying materials, not only thanks to better elastic and adhesive properties of the polymers, but also to a better interaction between binder and

active material [25,26]. The possibility to exploit inter- and intra-molecular polar interactions makes the choice of the binder particularly important for alloying materials [27,28].

It is therefore clear that the implementation of next-generation anode materials requires an in-depth study of the interfacial and structural behavior upon cycling to fully understand the mechanisms of Li^+ ions storage, especially when composite anodes contain a carbon matrix which yields a stabilizing effect and a non-negligible electrochemical activity. In this regard, ex-situ and in-situ spectroscopic techniques are fundamental to evaluate the evolution of structural, electrochemical and kinetic properties of electrode materials [29–32].

Herein, we report the preparation and characterization of a Si/Hard Carbon composite anode from waste biomass (Corn Cobs) via a simple route and without the use of activating agents, combined with the use of a sustainable crosslinked Chitosan-based binder. The composite electrode is prepared by employing a relatively high Si content, with a Si:HC ratio of 3:5 (i.e. 37.5 % Si in the active material) in order to provide a good balancing between structural stability and electrochemical performance, especially when considering that commercial Si/Graphite anodes still cannot go beyond a Si mass content of 10-15 % to maintain electrode integrity [33,34]. The crosslinked chitosan-based binder is prepared according to a method reported in literature [27] and employed as a greener alternative to commercial polyvinylidene fluoride (PVdF). Thanks to the synergistic effect of the Hard Carbon containment matrix and the crosslinked Chitosan-based binder, the electrode shows a high and stable specific capacity at a rate of 1 A g^{-1}, together with a very good rate capability and capacity retention. An extensive structural, interfacial and electrochemical characterization of the material is also reported, which includes ex-situ Raman spectroscopy, impedance measurements and calculation of the distribution of relaxation times (DRT), performed during both lithiation and de-lithiation processes.

2. EXPERIMENTAL SECTION

2.1 Materials. Chitosan (low molecular weight, Sigma-Aldrich), Citric Acid monohydrate (Sigma-Aldrich), Sodium Carboxymethyl Cellulose (MW ≈ 250000, Sigma-Aldrich), Sodium Alginate (Sigma Aldrich), Polyacrylic Acid (MW ≈ 450000, Sigma-Aldrich), Si (APS ≈ 100nm, Plasma Synthesized, Alfa Aesar), Super C-65 (Timcal) and Timrex KS15 Graphite (Timcal) were used as received. The electrolyte LP30 +5% vinylene carbonate (VC) was pre-formulated by Solvionic (Tolouse, France) and used as received.

2.2 Synthesis of Corn Cobs-Derived Hard Carbon. The hard carbon from Corn Cobs biowaste (labeled as CCDHC) was prepared via a simple and easy-to-perform carbonization route under inert gas flow, without any acid/base pretreatment steps. The adopted procedure can be summarized as follows: the precursor was preliminarily ground, sieved (dimensions < 1mm) and annealed in a tubular furnace at 950 °C for 3 h under argon atmosphere, with a heating ramp of 5 °C min^{-1}. The as-obtained carbon was then finely ground through a planetary ball-mill for 30 min at 300 rpm in clockwise/counterclockwise mode, to reduce the particle size of the final CCDHC (50 mL steel jar with 3 steel balls of 20 mm diameter and ball-to-powder weight ratio of 15:1).

2.3 Electrode Processing. The slurry for the preparation of Si/CCDHC and Si/Graphite (Si/Gr) composite electrodes, and for bare Si electrodes, were obtained by mixing all the components in the formulation of 80:15:5 (active material : binder : conductive carbon Super C-65), with a 3:5 w/w ratio between Si and CCDHC. The chitosan/citric acid (CS/CA) binder solution was firstly prepared by dissolving chitosan in a 1 % acetic acid solution, and separately adding a proper amount of citric acid solution to obtain a 9:1 w/w ratio (Chitosan : Citric acid) between the two components. Polyacrylic acid (PAA), sodium carboxymethyl cellulose (CMC)

and sodium alginate (Alg) were dissolved in ultrapure water and used to assess the influence of the binder on the Si/CCDHC composite. The active material (Si/CCDHC, Si/Gr or bare Si) and the carbon additive were ground and mixed through a planetary ball-mill for 30 min at 200 rpm in clockwise/counterclockwise mode, added to the binder solution and left stirring overnight through a magnetic stirrer. The as-obtained slurries were casted onto copper foil (10 μm thickness) through doctor blading technique with a wet thickness of 150 μm. Finally, the electrode layers with the CS/CA binder were dried at 150 °C for 2 h in order to thermally induce condensation between the binder components, while those containing the other binders were dried at 70°C for 2h. Circular electrodes of Ø = 9 mm and Ø = 16 mm were cut by using two electrode punchers (EL-CELL), pressed at 7.86 ton cm^{-2} through a hydraulic press, weighed and eventually vacuum-dried at 120 °C overnight. The mass loadings of the active material ranged 1.0 to 1.2 mg cm^{-2} for all the tested electrodes.

2.4 Structural, Chemical and Morphological Characterization. Infrared spectroscopy (Perkin-Elmer Frontier FTIR) was employed on two films of the sole binder (casted and dried at 60 °C and 150 °C respectively) to confirm the presence of the amide functional group resulting from the condensation. For the measurement, mixtures only containing chitosan and citric acid in a 9:1 w/w ratio were prepared in a 1 % acetic acid solution and left stirring for 12 h; afterwards, both solutions were casted onto polytetrafluoroethylene (PTFE) foil and dried at the target temperatures for comparison. The morphologies of CCDHC, of the Si/CCDHC composite, and of electrodes prepared with different binders (pristine and after cycling) were studied using scanning electron microscopy (Zeiss Sigma 300 FE-SEM equipped with Bruker QUANTAX EDX detector). The structure of the obtained materials was characterized by means of Raman spectroscopy (Horiba IHR 320, λ = 532 nm) and powder X-ray diffraction (Philips

diffractometer equipped with a Cu-Kα source, λ = 1.540 Å). A thermogravimetric analysis (Perkin-Elmer STA6000 TGA-DTA) was performed on the Si/CCDHC composite under oxidative conditions to confirm the 3:5 ratio between Si and CCDHC after ball-mill.

2.5 Electrochemical Measurements. Most of the electrochemical measurements for the Si/CCDHC anode were carried out by using three-electrode Swagelok-type polypropylene cells, with lithium metal (Sigma Aldrich) serving as both counter and reference electrode. For the impedance measurements of electrodes with different binders, the Swagelok-type polypropylene cells were employed in a two-electrode configuration, since the contribution of Li metal to the total resistance at the fully de-lithiated state is expected to be negligible. Two-electrode CR2032 coin-type cells were employed for the impedance measurements performed through a "staircase" protocol, in order to avoid the presence of inductive loops, especially at low potentials. Whatman GF/A fiberglass separators were used for all the measurements. All cells tested were assembled in a high-purity Argon-filled glovebox (Jacomex GP-Campus) with O_2 and H_2O content < 0.8 ppm). The electrolyte employed was 1M $LiPF_6$ dissolved in a 1:1 v/v mixture of ethylene carbonate and dimethyl carbonate (EC:DMC) with 5 % VC (w/w) additive. All electrochemical measurements were performed using a VMP-3 multichannel electrochemical workstation with an integrated frequency response analyzer by Bio-Logic. Prior to any electrochemical characterization, a 12-hour OCV period was used. Cyclic voltammetries (CV) were acquired at a scan rate of 0.1 mV s^{-1}. The composite's charge-discharge performance was evaluated by galvanostatic cycling with a constant current of 1 A g^{-1} for 100 cycles, applying a constant-voltage step at the end of each lithiation. The composite electrode employing commercial graphite (KS15) as the buffering matrix and the CS/CA binder, as well as the bare Si electrode, were tested in the same cycling conditions. A rate capability test was performed by galvanostatic

cycling the material with specific currents ranging from 0.1 A g^{-1} up to 4.0 A g^{-1}. All the cycling tests were performed within the voltage window 0.01 V < E < 1.50 V. Electrochemical impedance spectroscopy (EIS) measurements were acquired upon cycling in potentiostatic mode during 1st cycle and every 10th cycle at a fixed bias potential E = 0.4 V. Moreover, impedance measurements were also carried out on electrodes with different binders at OCV and at a bias potential of E = 1.5 V after 1 and 10 charge/discharge cycles. Finally, "staircase" impedance measurements were carried out within a single cycle (10th cycle) at different states of charge (SoC) during both lithiation and de-lithiation, with a sampling interval of 0.02 V. For all the EIS measurements, a sinusoidal perturbation of $\Delta E = \pm 5$ mV was applied over the frequency range 10 mHz < f < 199 kHz, with 10 points per decade and logarithmic spacing. For the "staircase" impedance measurements, the low-frequency diffusion region was subtracted from the obtained Nyquist plots in order to calculate the function of distribution of relaxation times (DRT). The fitting procedures by Equivalent Circuit Method (ECM) and the calculation of the DRT function (Tikhonov regularization, $\lambda = 10^{-4}$) were performed by using the software RelaxIS3. All the potential values are referred to the Li^+/Li redox couple (E° = -3.04 V vs. RHE).

Ex-situ Raman measurements were performed on samples charged/discharged to different states of charge during the first cycle. The cells were galvanostatically cycled at a specific current of 1 A g^{-1} until a certain state of charge and then equilibrated by applying a constant voltage for 6 h. The cells were subsequently disassembled in the glovebox under Ar atmosphere, and each electrode was washed three times in dimethyl carbonate (anhydrous, Sigma Aldrich) to remove any electrolyte residues which could generate interferences in the Raman measurements. The electrodes were eventually sealed by epoxy resin between two microscope slides to prevent unwanted reactions with air and moisture during the analysis.

3. RESULTS AND DISCUSSION

3.1 Chemical and Structural Analysis of the Binder. Prior to cell assembly, a chemical and structural analysis was carried out on two films of the sole binder dried at different temperatures (i.e. 60 °C and 150 °C), to verify the crosslinking reaction between chitosan and citric acid. The FTIR spectra of the two films are shown in **Figure 1**.
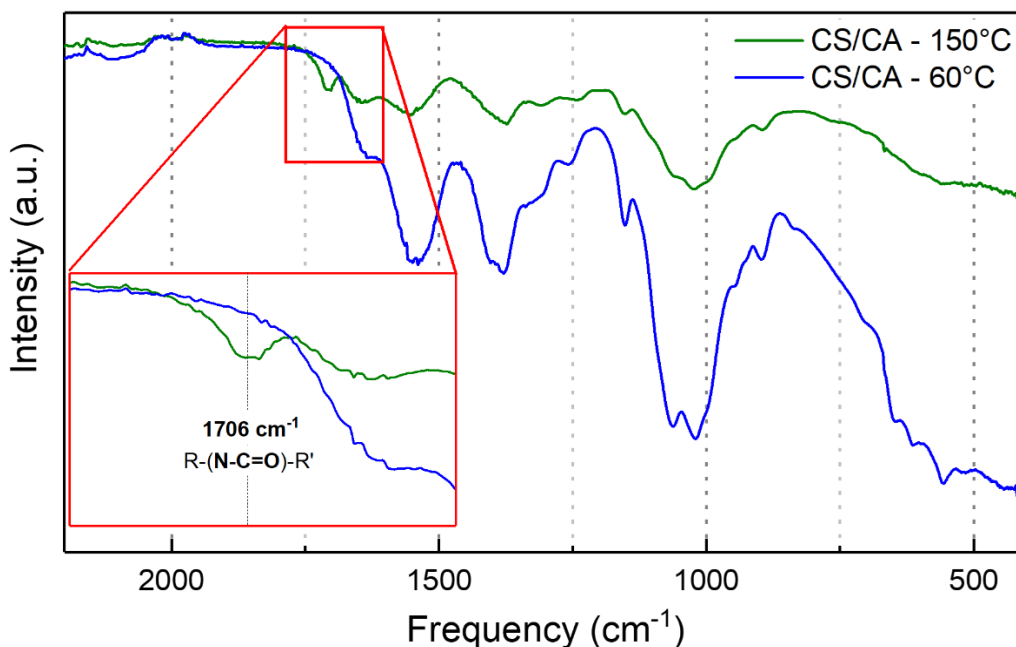

Figure 1. FTIR spectra of the binder polymeric film heated at 60 °C (blue) and 150 °C (green). The inset shows the peak related to the formation of the amide bond from condensation.

The FTIR spectra recorded for both samples are consistent with other results reported in literature [27], and the main signals are summarized in **Table 1**. In particular, both samples display the characteristic signals corresponding to the deformation vibrations of primary and secondary amines between 1500 and 1600 cm^{-1} arising from chitosan. However, after heat-treating the sample at 150 °C, an additional feature at about 1706 cm^{-1} appears (see inset in **Figure 1**), clearly indicating the formation of the N-C=O amide bond. The presence of a proper covalent bonding between the free deacetylated amine of chitosan and the carboxyl groups of citric acid

indicates that the thermally induced condensation reaction successfully occurred, resulting in the interconnection of chitosan chains through bridging citric acid.

Peak position	Associated bond
894 cm^{-1}	Primary **N-H**
1022 cm^{-1}	**C-O-C**
1062 cm^{-1}	Secondary **C-O**H
1152 cm^{-1}	**C-O-C**
1254 cm^{-1}	Secondary R$_2$C**O-H**
1300-1450 cm^{-1}	**C-H**
1500-1600 cm^{-1}	Primary RH**N-H** and secondary R$_2$**N-H**
1649 cm^{-1}	**C-N**
1706 cm^{-1}	R(**N-C=O**)R'

Table 1. Summary of the FTIR main signals and associated bonds of the polymeric binder films.

3.2 Structural and Morphological Characterization of Si/CCDHC. The structure, morphology, and composition of the synthesized carbon (CCDHC) and of the composite Si/CCDHC were investigated by means of Raman spectroscopy, X-ray diffraction (XRD), scanning electron microscopy (SEM) and EDX analysis, as reported in **Figure S1** and **Figure 2**, respectively.

The Raman spectrum of CCDHC (**Figure S1a**) displays the presence of the two characteristic bands of disordered carbons: the D band at 1337 cm^{-1} and the G band at 1587 cm^{-1}, associated with the breathing mode of A$_{1g}$ symmetry and with the in-plane bond-stretching motion of pairs of C sp^2 atoms of E$_{2g}$ symmetry, respectively. The former mode is not active in pure graphite and only becomes active in the presence of structural defects, while the latter is typical of ordered

graphitic sites. Hence the intensity ratio I_D/I_G can provide an indication of the degree of disorder of the hard carbon [35,36]. For CCDHC this ratio was calculated to be 1.003, suggesting a highly disordered structure with the presence of defects. Additionally, in the region 2500-3200 cm^{-1}, the second order bands associated to 2D (characteristic of graphitic domains) and D+G (characteristic of defect-activated scattering) bands are visible [37]. The XRD pattern in **Figure S1b** shows the presence of a clear signal at $2\theta \approx 24°$ corresponding to the (002) plane, and a weaker signal at $2\theta \approx 43°$ corresponding to the (100) plane, both related to graphitic-like domains. The (002) band indicates the spacing between graphene layers in the graphitic domains, and the broadening of the signal is consistent with the presence of short-range structures composed of a random layer lattice with defective sites and crystalline graphitic domains [38]. The graphitic domain size (L_a) for the hard carbon sample was calculated from the Raman spectrum according to **Eq. S1**. From the XRD pattern, the diffraction peak in the plane (002) was used to calculate the interlayer spacing (d_{002}) and the stacking height (L_c), by using Bragg's Law (**Eq. S2**) and Scherrer's equation (**Eq. S3**), respectively. Finally, an estimation of the number of graphene stacking layers (n) was obtained by dividing the stacking height L_c by the interlayer spacing d_{002}. Details on the calculations can be separately found in the Supporting Information. All the values obtained by Raman spectroscopy and X-ray diffraction are summarized in **Table 2**, and are in line with the literature data of hard carbons possessing amorphous regions mixed with graphitic domains [36,38].

Sample	I_D/I_G	La (nm)	d_{002}	L_c (nm)	n
CCDHC	1.003	19.17	0.387	0.89	2.30

Table 2. Summary of the crystallographic parameters obtained by Raman spectroscopy and X-Ray diffraction.

The SEM micrographs of the hard carbon powder (**Figure S1c**) show the presence of large, aggregated clusters with a block-like morphology, composed of smaller nanoparticles. A certain degree of graphitization can be visually discerned by the presence of some lamellar-like structures composing the graphene stacking sheets. The EDX analysis in **Figure S1d** finally shows that despite the absence of acid leaching, the only observable impurity from the starting biomass after annealing is traces of K, probably in the form of K_2O. The low intensity of the signal from O atoms indicates a very low surface functionalization of the obtained hard carbon.
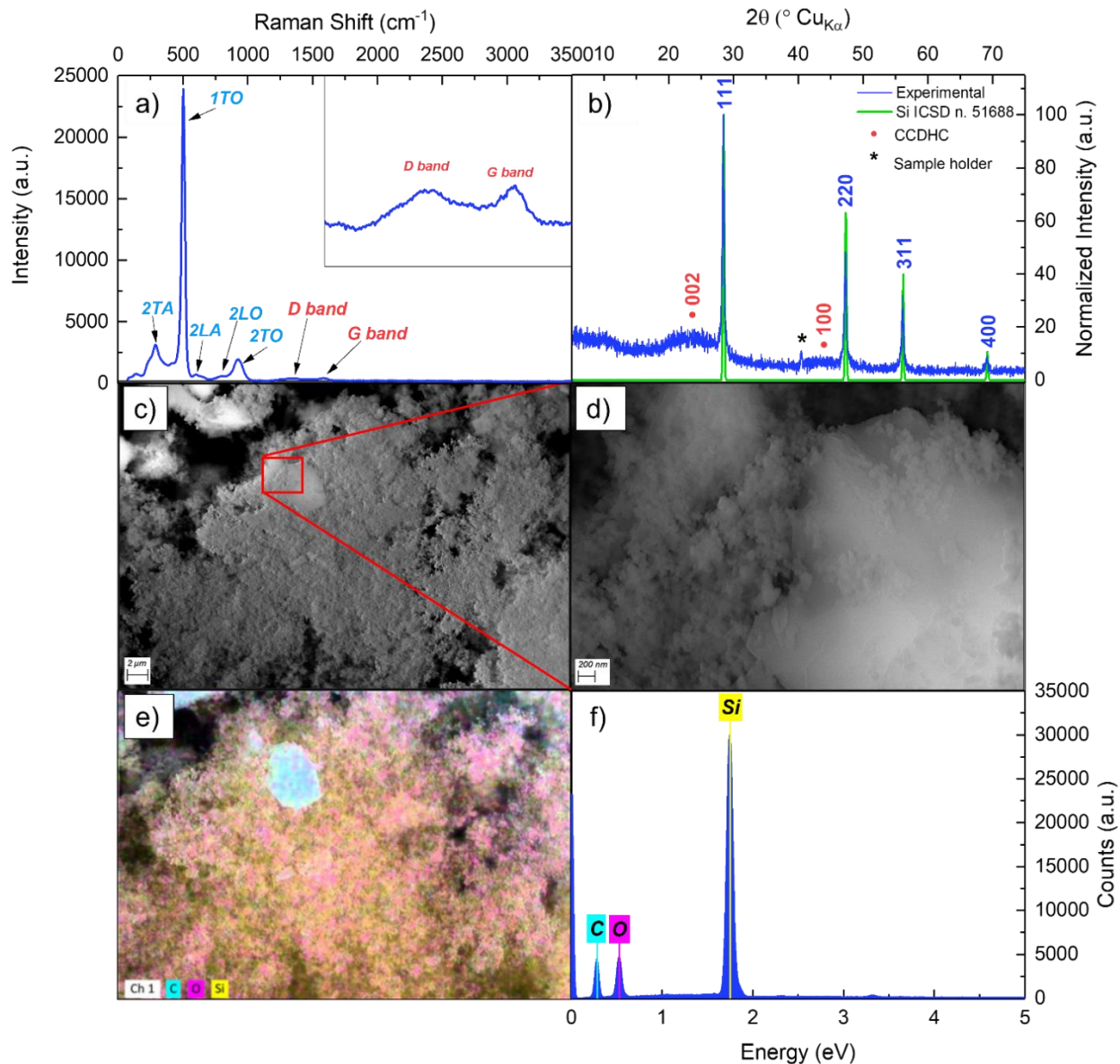
Figure 2. a) Raman spectrum of Si/CCDHC, with magnification on the D and G bands (inset); b) Experimental diffraction pattern of Si/CCDHC (blue) and reference diffractogram of Si (green); SEM micrographs of Si/CCDHC at c) 5000x and d) 40000x magnifications; e) Elemental mapping of Si/CCDHC for Si, C and O; f) EDX analysis of Si/CCDHC.

The Raman spectrum of the Si/CCDHC powder after ball-mill (**Figure 2a**), is consistent with literature findings for Si and hard carbon matrix. Specifically, the peak at 520 cm^{-1} can be ascribed to the first order transverse optical mode (1TO) typical of c-Si; the bands at 300 cm^{-1},

609 cm^{-1}, 808 cm^{-1} and 930 cm^{-1} are consistent with the second order transverse acoustic (2TA), longitudinal acoustic (2LA), longitudinal optic (2LO) and transverse optical (2TO) modes of Si, respectively [39]; the D and G bands of CCDHC are also slightly visible at 1339 cm^{-1} and 1589 cm^{-1}, while the second order 2D and D+G fall within the background due to the very high intensity of Si-related peaks. The crystallinity of Si is confirmed by calculating the value of the integrated intensity ratio between the second and first order transverse modes (I_{2TO}/I_{1TO}), which is reported to be close to 0.25 for a-Si and decreases to 0.1 for bulk c-Si: the obtained ratio of 0.083, indicates a crystallinity similar to that reported for bulk c-Si. However, the positions of the 2TO and 2LO modes (here 808 and 930 cm^{-1}) are found to be slightly shifted to lower wavenumbers with respect to those reported for the bulk c-Si (namely 825 and 940 cm^{-1}), consistently with the presence of some nanocrystals with dimensions in the range of 5-7 nm [40–42]. The experimental diffraction pattern of Si/CCDHC, reported in **Figure 2b**, is consistent with the presence of cubic Si with space group Fd3m (ICSD n. 51688). A crystallite size of ≈ 109 nm was calculated by applying **Eq. S3** (Scherrer's equation). This value is in line with the particle dimensions declared by the supplier. The peaks at 2θ ≈ 24° and 2θ ≈ 43° are consistent with the diffraction pattern shown in **Figure S1b** for the bare CCDHC powder. The small peak labeled as (*) is addressed to the brass sample holder used for the analysis. **Figure 2c-e** shows the SEM micrographs of the Si/CCDHC composite at different magnifications and the elemental mapping of Si, C and O performed on the same spot. At higher magnifications (**Figure 2d**), it is possible to observe that the Si nanoparticles visually possess a spherical morphology with a particle size of about 100 nm, which is consistent with the calculated crystallite size from the structural characterization. By comparing the micrograph obtained at low and high magnification (**Figure 2c-d**) with the elemental mapping (**Figure 2e**), Si and CCDHC can be properly distinguished, as the small Si

particles seem to be lying either onto the rough surface of the larger clusters of hard carbon or between chunks. From the SEM micrograph in **Figure S1c**, the lamellar-like structures and the big cavities on the rough surface of CCDHC may act as sites where most of the Si can be accommodated, being Si particles much smaller than those of the Hard Carbon; we thus believe that this could provide a reasonable buffering activity for Si volume expansion upon cycling. Moreover, if compared to **Figure S1d**, the presence of homogeneously distributed O atoms throughout the whole sample suggests that Si particles do possess a slight degree of surface oxidation. This is also confirmed by the more pronounced intensity of the related EDX peak in **Figure 2f**, suggesting a higher O content than bare CCDHC (O peak becomes comparable to the C one). For the sake of clarity, from **Figure 2f** one could argue that the intensity of Si peak seems to be much higher than that of C, thus indicating a much higher amount of Si related to C. However, in the absence of a flat- and highly polished-surface standard, a proper quantification of Si and C cannot be performed: lighter elements (i.e. O and C) generally yield low-energy photons which are susceptible to self-absorption phenomena when an energy beam $E_0 > 3$ keV is employed for the measurement. This phenomenon can lead to a lowering of the intensity of the C peak relative to that of Si, thus underestimating the amount of C when considering relative intensities [43]. Hence, in order to provide a more accurate measurement, a TGA analysis was performed on the composite powder to assess the Si/C composition after ball-milling (**Figure S2**). The results from TGA indicate a small initial weight loss of about 6.5 % in the range 30-100 °C, which can be attributed to the moisture from the atmosphere. The subsequent pronounced mass loss of about 57.5 % in the range 400-600 °C is consistent with the oxidation of CCDHC to CO_2, while the remaining 36% mass is attributed to Si. This result provides confirmation of the

3:5 w/w ratio between Si and C and indicates a homogeneous mixing of the components after ball-milling.

3.3 Electrochemical Characterization. In order to investigate the redox processes occurring during Li storage and assess the effect of the carbon matrix upon cycling, electrodes of Si/CCDHC were subjected to cyclic voltammetry (CV) at a scan rate of 0.1 mV s^{-1} and galvanostatic cycling within the potential window of 0.01-1.50 V in half-cells vs. Li. The electrochemical behavior was compared with electrodes of Si/Graphite (Si/Gr) prepared in the same way and with comparable active material mass loading. The electrochemical behavior of the bare hard carbon matrix is shown in **Figure S3**, in terms of both cyclic voltammetry and galvanostatic cycling. Furthermore, the electrochemical performance of bare Si employing the CS/CA binder is also given for comparison in **Figure S4**, in order to assess the superiority of the Si/CCDHC composite.

The voltammograms acquired during the first and second cycle for the two composites are reported in **Figure 3a-b**. During the cathodic and anodic scans, the characteristic features of lithium storage by Si can be observed, as well as the signals related to the lithiation of the different carbon matrices and to SEI formation. As for the Si/Gr composite (**Figure 3a**), during the first cathodic scan, the small peak at 1.23 V (D$_1$) and the broad peak at 0.75 V (D$_2$) can be attributed to the irreversible decomposition of VC from the electrolyte and formation of the passivation layer, respectively [44,45]; the peak at 0.20 V (G$_1$) is related to the first stage of intercalation of Li$^+$ ions into graphite, with formation of LiC$_{24}$ phase, while the sharp peak ranging from 0.13 V to 0.01 V (G$_2$+S$_1$) can be assigned to the superposition of the different lithiation phases of graphite (from LiC$_{24}$ to LiC$_{18}$, LiC$_{12}$ and finally LiC$_6$) and the alloying of Si with phase transition to amorphous Li$_x$Si and crystalline Li$_{15}$Si$_4$ phases. Upon the first anodic

scan, the three close peaks ranging from 0.11 V to 0.27 V are related to the stepwise de-intercalation of Li from graphite, with reformation of the phases LiC_{12} (G_3), LiC_{18}/LiC_{24} (G_4), and complete delithiation to C_6 (G_5); the peaks at 0.34 V (S_2) and 0.47 V (S_3) can be assigned to the de-alloying of the amorphous Li_xSi phases and dissolution of $Li_{15}Si_4$ phase with amorphization of the resulting Si. From the second cathodic scan Si lithiation proceeds mostly through formation of amorphous Li_xSi phases, which endmember corresponds to $Li_{13}Si_4$ stoichiometry as evidenced by the small hump visible at 0.21 V (S_4) [45–48]. As for the Si/CCDHC (**Figure 3b**), during the first cathodic scan, the peaks related to the irreversible decomposition of VC (D_1) and formation of SEI (D_2) are also present. The peak ranging from 0.13 V to 0.01 V (C_1+S_1) can be attributed to both insertion of Li^+ ions between the graphene planes of the disordered carbon [49], and to alloying reaction of Si to Li_xSi and $Li_{15}Si_4$ phases. Upon the first anodic scan, the small hump at 0.08 V (C_2) indicates the de-insertion of Li from the hard carbon matrix, while the peaks at 0.35 V (S_2) and at 0.47 V (S_3) are consistent with the de-alloying process and dissolution of the higher lithiated state, as observed in the Si/Gr composite. From the second cycle, the electrochemical signal related to Si lithiation processes, already evidenced in **Figure 3a**, are confirmed. All the carbon-related peaks are consistent with the cyclic voltammetry reported in **Figure S3a**. No additional processes are evidenced after the second cycle for both composites.
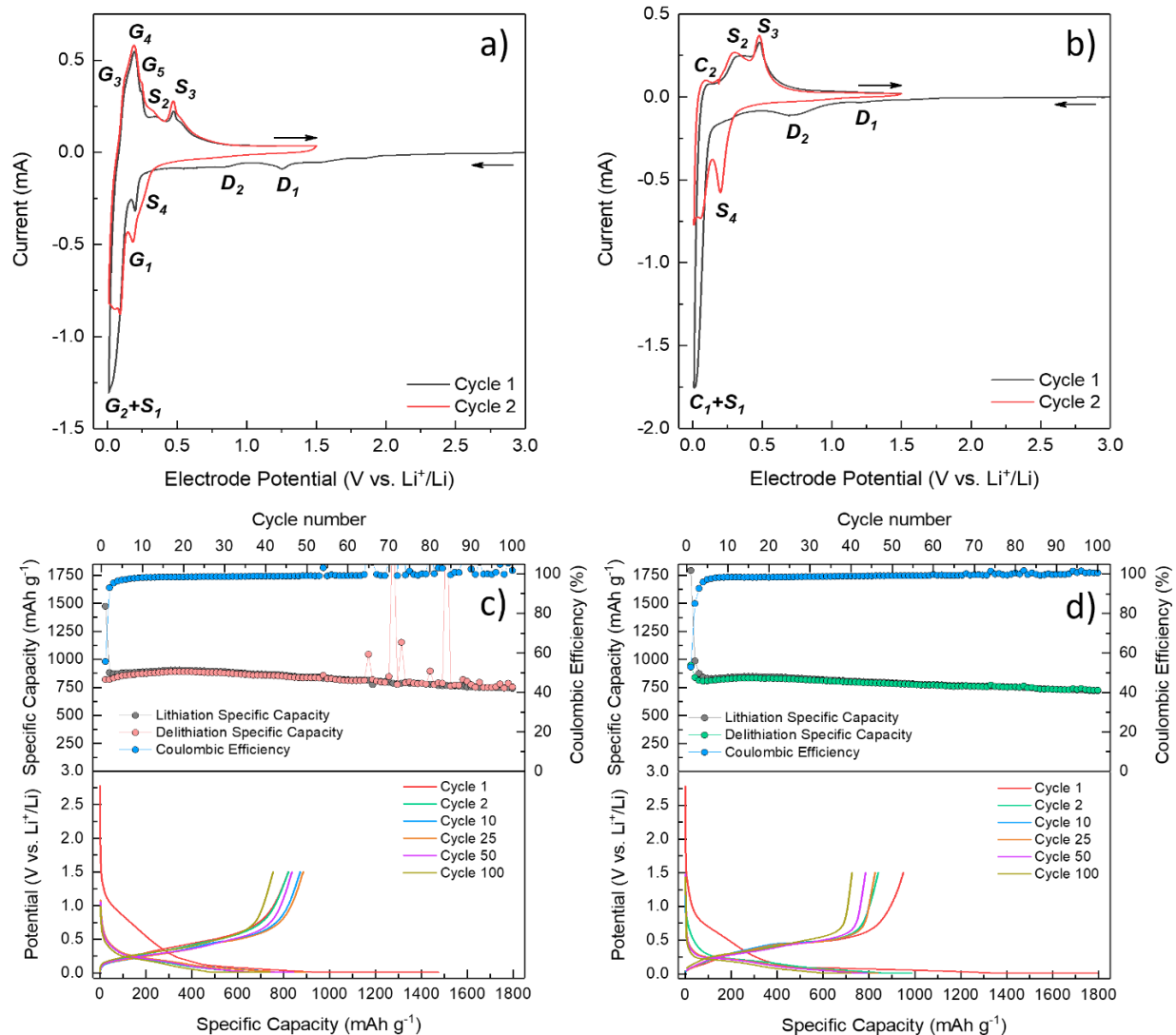
Figure 3. Cyclic voltammetry of the first two cycles for a) Si/Gr and b) Si/CCDHC; galvanostatic cycles and E vs. Q profiles obtained at 1 A g^{-1} current density for c) Si/Gr and d) Si/CCDHC. Both composite electrodes employ the CS/CA binder.

The charge/discharge performance over 100 cycles and the stability of the Si/CCDHC composite have been evaluated by galvanostatic cycling at 1 A g^{-1} in the 0.01 V < E < 1.5 V potential window, and compared to the benchmark Si/Gr composite cycled in the same conditions. The specific capacities obtained for both electrodes are reported in **Figure 3c-d**, as well as the related coulombic efficiencies. Both composites show a high initial capacity decay mainly due to two

irreversible processes: the formation of the solid electrolyte interphase and the amorphization of the initial crystalline silicon. As it can be visualized from both potential profiles and galvanostatic cycles, these processes mainly occur during the first cycle, leading to poor initial coulombic efficiency of 55.94 % and 53.24 % for Si/Gr and Si/CCDHC, respectively, with a progressive increase in reversibility starting from the 5th cycle on, after which the specific capacity tends to stabilize at about 800 mAh g^{-1} for both materials. Despite the slightly lower initial coulombic efficiency of Si/CCDHC with respect to the benchmark Si/Gr electrode, the average coulombic efficiency of the latter stabilizes at about 98.8 %, while that of Si/CCDHC can reach values up to 99.4 %, thus indicating a better reversibility of the processes after the first cycles. Moreover, after 64 cycles the benchmark Si/Gr electrode starts experiencing high spikes in the delivered capacity during the oxidation process, suggesting breakage and reformation of SEI as a result of the structural shrinkage of Si particles upon de-alloying [50]. This behavior is not encountered with the Si/CCDHC composite during the entire test, indicating that the hard carbon matrix is able to mitigate the effects of the volume changes upon cycling and to maintain a good structural integrity of the electrode. For comparison, the cycling behavior of a bare Si electrode with the CS/CA binder (**Figure S4a-b**) is also provided, and it clearly shows the typical capacity decay of Si in the absence of a buffering matrix, further confirming the superiority of the Si/CCDHC composite especially in terms of stability.

The effect of the crosslinked binder was also studied by comparing the cycling performance of Si/CCDHC electrodes fabricated with different binders, maintaining the same electrode formulation and cycling conditions (**Figure 4**).
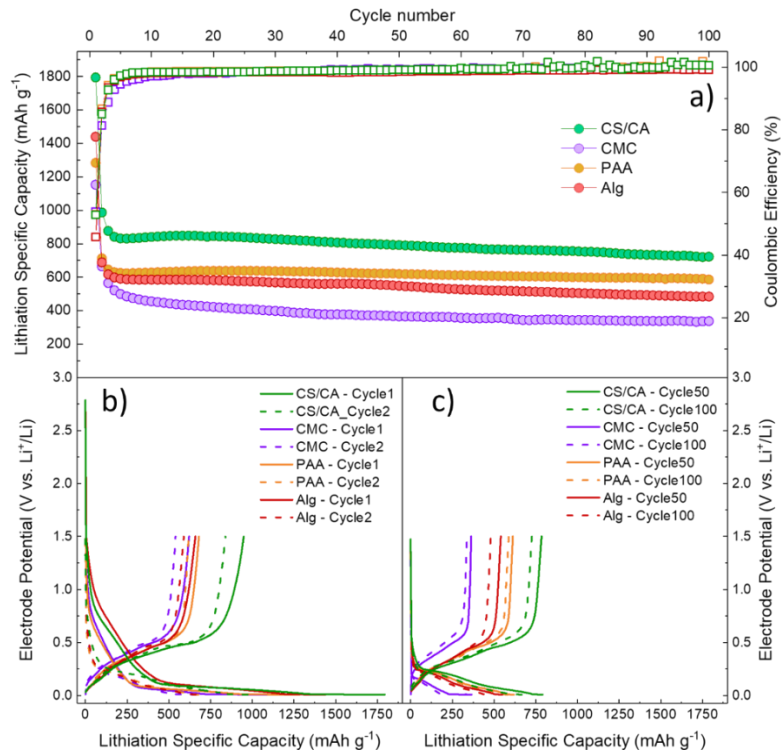
Figure 4. a) Comparison of galvanostatic cycling of Si/CCDHC employing different binders at 1.0 A g-1 (CS/CA = green, CMC = violet, PAA = orange, Alg = red); E vs Q profiles at b) 1st and 2nd cycle, and c) 50th and 100th cycle, for each binder employed.

Notably, from the data reported in **Figure 4a**, the crosslinked CS/CA binder shows improved performance and stability with respect to all other binders studied for the comparison (i.e. PAA, CMC and Alg). The results obtained clearly demonstrate the beneficial effects from the combination of the hard carbon matrix and the crosslinked binder in promoting a higher stability with respect to conventionally studied components, resulting in better performance and slower capacity decay, as evidenced in the potential profiles in **Figure 4b-c**.

A morphological investigation by SEM was also carried out on pristine (**Figure 5a-d**) and cycled electrodes (**Figure 5e-h**) in order to obtain additional information about the electrode integrity after repeated cycling. Impedance measurements were also performed at OCV, after 1 cycle and

after 10 cycles for all electrodes, to further prove the ability of the CS/CA binder to improve the electrode stability upon cycling (**Figure 5i-k**).
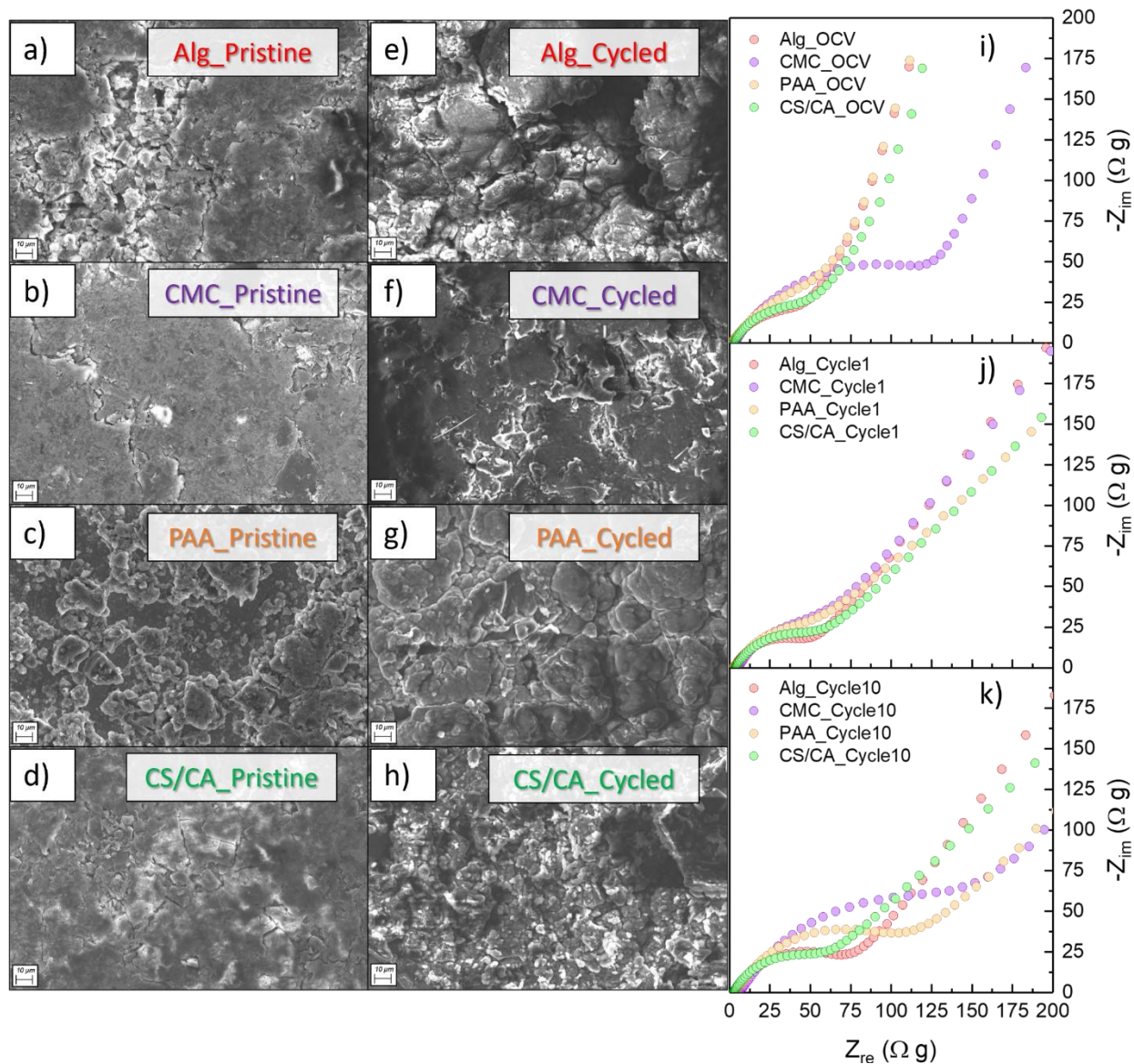
Figure 5. SEM micrographs at 1000x magnification of pristine Si/CCDHC electrodes employing a) Alg, b) CMC, c) PAA and d) CS/CA binders; SEM micrographs at 1000x of Si/CCDHC electrodes after 100 cycles employing e) Alg, f) CMC, g) PAA and h) CS/CA binders; EIS performed on all electrodes at i) OCV, j) cycle 1 and k) cycle 10.

The morphologies of the pristine electrodes in **Figure 5a-d** show different textures according to the binder employed: in particular, the PAA-based electrode displays a very rough surface and

higher inhomogeneity in the spatial distribution of particles compared to the other electrodes, which have a more homogeneous distribution and a flat surface. Moreover, the Alginate-based electrode visually displays a higher number of cracks with respect to the CMC- and the Chitosan-based ones, which possess a relatively flat surface. After 100 cycles (**Figure 5e-h**) all electrodes show some degree of agglomeration: the electrodes based on Alginate, CMC and PAA all show a very high particle agglomeration after cycling, with the formation of big clusters; in turn, the Chitosan-based electrode displays a less pronounced agglomeration, with smaller clusters and a more homogeneous particle distribution. This indicates that the CS/CA binder is able to favor a better adhesion with the current collector and cohesion between Si particles, which are more homogeneously kept close to each other avoiding the formation of isolated clusters. This evidence is further supported by the impedance measurements in **Figure 5i-k**, which show the tendency of the CS/CA binder to favor a lower and more stable total impedance (diameter of semicircle) upon cycling.

The rate capability was evaluated in order to assess low- and high-current tolerance of the Si/CCDHC composite anode. In detail, specific currents of 0.1, 0.2, 0.5, 1.0, 2.0 and 4.0 A g^{-1} have been applied, with current rate changing every 5th cycle; subsequently, a specific current of 1.0 A g^{-1} was restored and kept for 150 cycles in order to verify the capacity retention of the material. No constant voltage step was applied at the end of the lithiation. The results of the rate capability test are shown in **Figure 6a-c**.
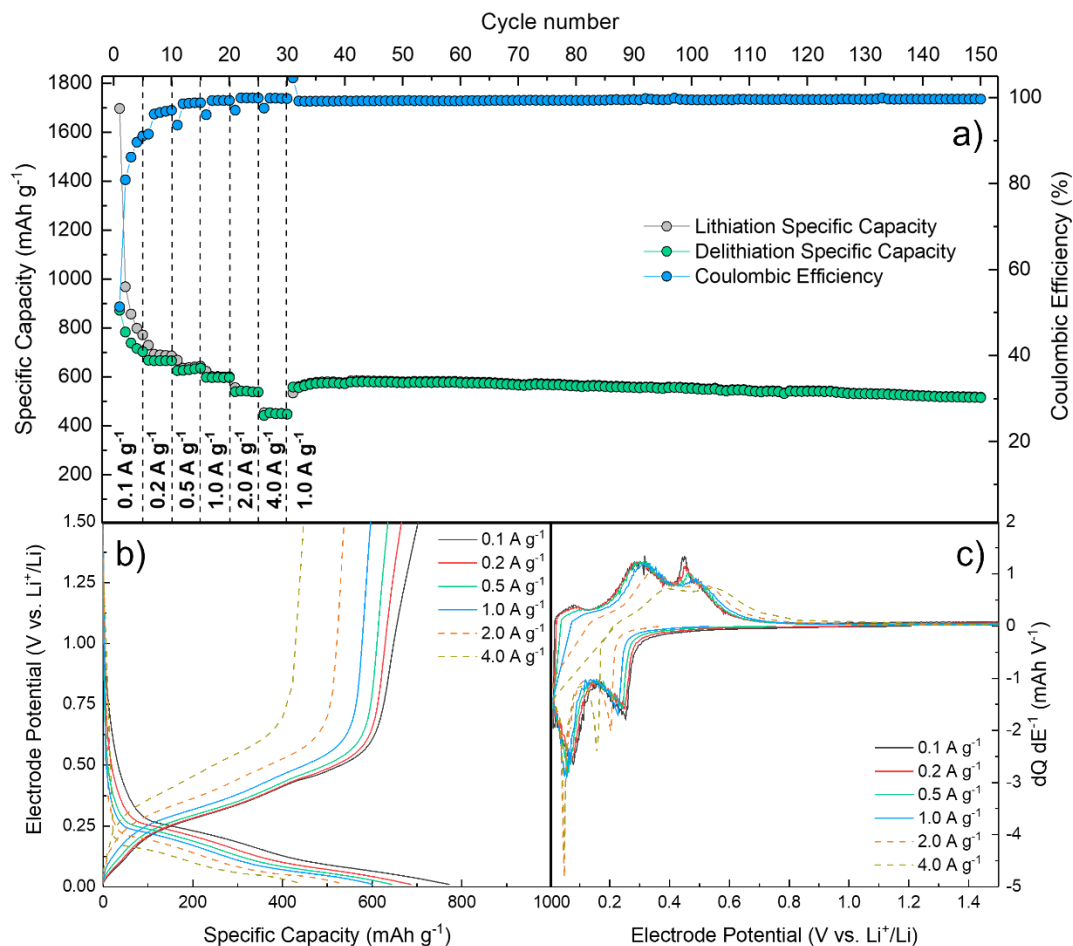
Figure 6. Rate capability of Si/CCDHC with CS/CA binder: a) Cycle number vs. Specific capacity/Coulombic efficiency; b) E vs. Q potential profiles for each specific current applied; c) Differential dQ dE^{-1} vs. E profiles for each specific current applied.

The specific capacity of the material only slightly decreases with increasing current rate up to 1.0 A g^{-1}, and the decrease becomes more pronounced for the higher rates. However, from the 6th cycle on, by progressively increasing the specific current applied up to 10 and 20 times (i.e. from 0.2 to 2.0 and 4.0 A g^{-1}) the capacity retention displayed by the composite is still of 77 % and 63 %, respectively. Moreover, the capacity retention of the material at the highest current rate tested is as high as 75 % when considering the standard cycling conditions at 1.0 A g^{-1} as the reference current rate confirming, the ability of the material to sustain high specific currents. When the

current of 1.0 A g^{-1} is restored, the specific capacity is recovered and maintained for 120 cycles at values comparable to those previously obtained at the same rate, thus further demonstrating an excellent capacity retention. Notably, the coulombic efficiencies are lower at slow currents (i.e. 0.1 A g^{-1}), but progressively increase at higher specific currents up to nearly 100 % when 4.0 A g^{-1} is applied. This result suggests that, on one side lower currents facilitate the kinetics of irreversible interfacial processes, while on the other side the kinetics of the reversible (de)alloying process is favored at higher currents. In **Table 3**, the main characteristics of the electrodes tested in terms of mass loading, composition, rate capability performance, capacity retention at high specific currents and production of the C buffering matrix, are compared to some Si/C composites recently published [51–60]. It is worth to notice that, despite the lower performance with respect to some works present in literature, the Si/CCDHC composite displays a higher capacity retention when going from slow to high current rates, while maintaining a higher active material mass loading and percentage in the electrode composition than many other materials considered hereby. In addition, the preparation of the CCDHC is kept as simple and sustainable as possible, thus offering promising scale-up opportunities.

Si-based composite	Electrode mass loading (mg cm^{-2}); Composition	Current rates considered (A g^{-1})	Specific capacity (mAh g^{-1}); Average capacity retention	Preparation of C matrix / buffering agent	Ref. (year)
Hierarchically C-coated Si	0.5 70:20:10	0.4 – 4.0	2900 – 1500 52 %	Resorcinol/Formaldehyde coating and annealing in Ar	[51] (2018)
Core-shell Si@Ni-NP@GNS	Not specified 60:20:20	0.2 – 1.0	1930 – 1107 57 %	GO coating and annealing in N$_2$ to obtain rGO	[52] (2018)
Si@void@C nanocomposite	0.24 – 0.44 60:20:20	0.2 – 4.0	1800 – 960 53 %	Resorcinol/Formaldehyde coating and annealing in Ar	[53] (2019)

Mesocarbon microbeads/nano-Si/amorphous C	2.0 80:10:10	0.2 – 1.0	≈720 – ≈350 ≈ 49%	Functionalization of C in HNO_3/H_2SO_4 solution; Annealing in Ar	54 (2019)
Nanoporous Si@Graphitized C	1.0 70:20:10	0.2 – 2.0	698 – 294 42 %	Magnesiothermic reduction in CO_2 flow	55 (2021)
Si/C/Graphite	1.0 – 3.0 50:25:25	0.2 – 2.0	697 – 487 70 %	Hydrothermal reaction at 160 °C Annealing in N_2	56 (2021)
N-doped C-coated hierarchically porous Si	1.5 70:20:10	0.2 – 2.0	925 – 435 47 %	Dopamine polymerization in HCl/Tris-buffer solution and annealing in Ar	57 (2021)
Si@RF@MP	1.0 80:10:10	0.2 – 2.0	≈610 – 421 ≈69 %	Resorcinol/Formaldehyde coating and heating at 370 °C in reactor Annealing in oxidative atmosphere and then Ar	58 (2022)
Si@C	Not specified 50:30:20	0.2 – 2.0	3019 – 2310 77 %	Annealing in N_2 with C_3H_6	59 (2022)
Si@GNCC	1.0 80:10:10	0.2 – 2.0	≈1750 – ≈1250 ≈ 71 %	C deposition via CVD from acetonitrile in Ar	60 (2022)
Si/CCDHC	**1.0 – 1.2** **80:15:5**	**0.2 – 1.0** **0.2 – 2.0** **0.2 – 4.0**	**690 – 600** **87 %** **690 – 535** **77%** **690 – 440** **63 %**	**Annealing of waste corn-cobs in Ar**	**This work**

Table 3. Comparison of electrode characteristics and rate performance of some Si/C composite anodes.

Finally, from the E vs. Q potential profiles in **Figure 6b** it is possible to observe that a low polarization is displayed by the material for all currents up to 1.0 A g^{-1}, indicated by the plateaus only slightly shifting to lower/higher potentials. This effect is even more clearly visualized in the calculated dQ dE^{-1} vs. E differential plots in **Figure 6c**, where the peaks related to the redox processes are almost completely superimposed with the exception of the highest current rates.

3.4 Characterization of Structural Evolution and Interfacial Properties. The structural stability and interfacial behavior of the material were investigated by means of ex-situ Raman spectroscopy and potentiostatic electrochemical impedance spectroscopy.

In order to verify the structural evolution of both Si and CCDHC matrix upon Li uptake/release, the first discharge/charge cycle has been studied through ex-situ Raman spectroscopy performed at selected electrode potentials. The potential values of interest correspond to the electrode being in the following conditions during lithiation (**Figure 7a**) and de-lithiation (**Figure 7c**) processes: (A) fresh electrode before SEI formation and alloying process (E = 1.0 V); (B) SEI formation (E = 0.7 V); (C) initial stages of Li-Si alloying and lithiation of the hard carbon matrix (E = 0.25 V); (D) complete formation of $Li_{15}Si_4$ alloy and full lithiation of the hard carbon matrix (E = 0.01 V); (E) de-lithiation of the hard carbon matrix (E = 0.085 V); (F) de-alloying of amorphous Si phases (E = 0.35 V); (G) dissolution of crystalline $Li_{15}Si_4$ phase (E = 0.48 V); (H) fully discharged and de-lithiated electrode (E = 1.5 V).
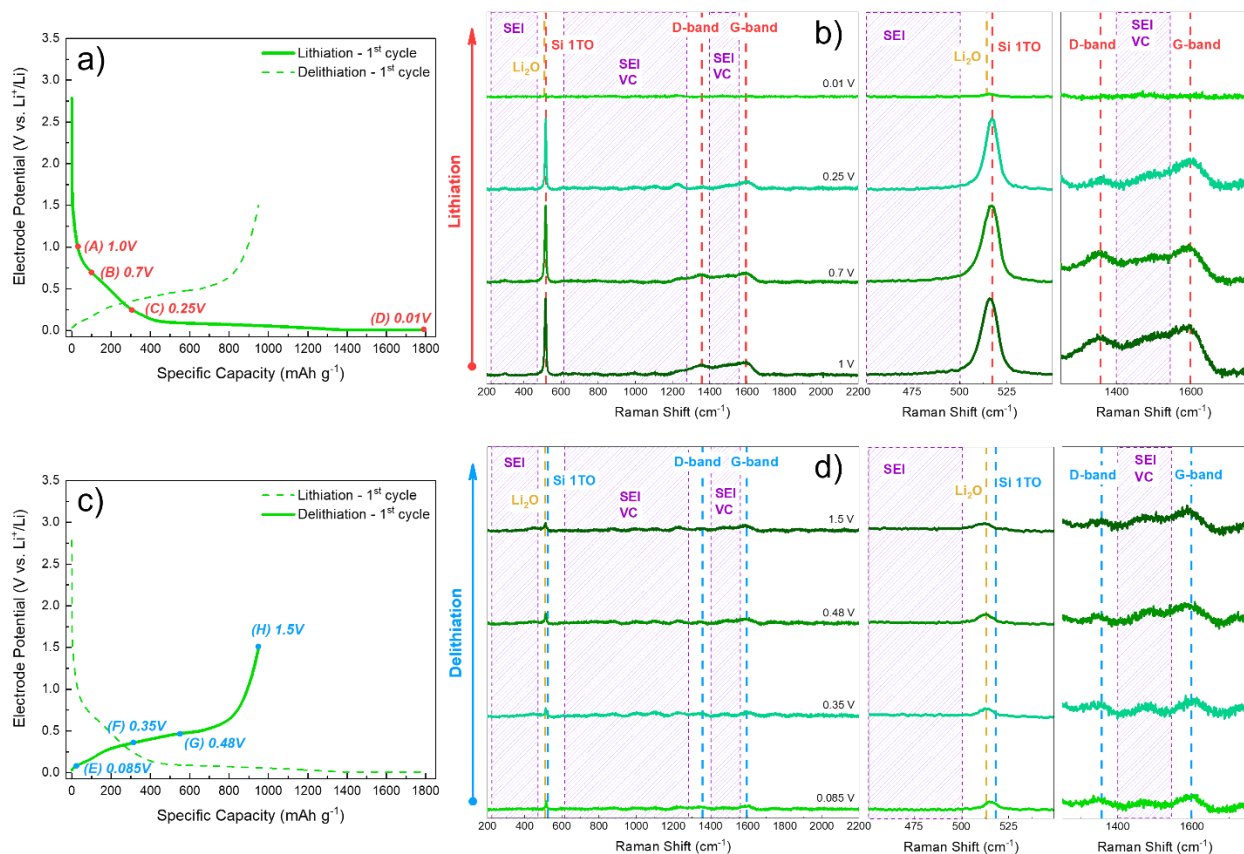
Figure 7. Ex-situ Raman characterization of Si/CCDHC electrodes with CS/CA binder: galvanostatic profiles with highlighted acquisition points during a) lithiation and c) de-lithiation; Raman spectra acquired during b) lithiation and d) de-lithiation, with magnifications on the Si 1TO and Li_2O peaks, and D/G bands of hard carbon.

During lithiation (**Figure 7b**), the spectra show the characteristic 1TO peak of crystalline Si at 920 cm^{-1} and the typical D and G bands from the hard carbon matrix and Super C-65 additive, located at 1357 cm^{-1} and 1598 cm^{-1}, respectively. Upon discharge, the intensity of the Si-related 1TO peak remains almost unchanged until very low potential values, and only at the lower cut-off (0.01 V) it is possible to observe the disappearance of the signal, indicating the conversion of crystalline Si to the $Li_{15}Si_4$ phase, which is Raman inactive. This phenomenon is in line with other findings in literature, and is addressed to the formation of Li-Si bonds upon lithiation (which disrupts the crystalline order of Si lattice) [61]. Generally, lithiation of Si is often accompanied by peak shift or broadening for the Si 1TO mode due to the stress induced in the

crystal structure [62]; in our case, none of these features is encountered at low potentials upon lithiation, indicating a good buffering activity from the hard carbon matrix and/or the crosslinked binder. In the last phase of the discharge, i.e. 0.01 V, a small peak is present at 515 cm^{-1}. At a first approximation this peak could be argued as a shift to lower wavenumbers of the 1TO mode of unreacted c-Si due to an induced stress from the lattice expansion of neighboring alloyed Si particles; however, since this peak is still present in the whole subsequent charge (**Figure 7d**), and no peak shift to higher wavenumbers is encountered until full de-lithiation (i.e. upon contraction and restoration of the Si crystal lattice), this possibility seems unlikely. Rather, this signal might be the result of Li reacting with the partially oxidized surface of Si particles (evidenced from the elemental mapping in **Figure 2e**) upon the first discharge, resulting in the irreversible formation of Li_2O [63]. Although the background is too high to observe any evidence of amorphous Si at 480 cm^{-1} [40] upon the charge process, the absence of Si-related peaks suggests amorphization of the resulting Si after the first cycle. In the 200-500 cm^{-1}, 600-1350 cm^{-1} and 1450-1500 cm^{-1} regions of the spectra, very low and enlarged signals can be observed, which are related with decomposition compounds from the electrolyte forming the passivation layer, mostly Li_2CO_3 from the carbonate solvents [62]. Interestingly, the SEI-related signals and the two peaks located at about 1000 cm^{-1} and 1475 cm^{-1} are already present at potentials higher than that of SEI formation upon discharge, and no obvious differences can be observed between 1.0 V and 0.7 V. Therefore, these features at 1.0 V can originate either from the binder [64] or more likely from the decomposition of VC [65], the latter occurring at potentials higher than 1.0 V. In **Figure S5** a Raman spectrum performed on a pristine electrode is reported: in the absence of electrolyte and of its related decomposition products, the Raman spectrum clearly shows the peaks related to Si 1TO and all the second-order vibrational modes as well as the carbon-related D and G band,

and neither SEI-related humps nor peaks at 1000 cm^{-1} and 1475 cm^{-1} can be observed in this case. Hence, the signals cannot be attributed to the binder. In particular, the peak at 1000 cm^{-1} is indeed assigned to a specific feature of VC-containing electrolytes, i.e. the R-O and C-C stretching modes of polycarbonates related to a radical polymerization of VC, as reported in another study [65]. The peak at 1475 cm^{-1} can be associated to one of the vibration modes of CO_3^{2-}, which may also be related to a ring opening reaction and a subsequent radical polymerization encountered in carbonate species [62,65–67]. As for the D and G bands, upon lithiation it is possible to observe a progressive decrease in intensity for both signals, which starts before the disappearance of the 1TO mode of Si, as the lithiation of C starts at slightly higher potentials. The decrease of the D band can be explained from the occupancy of defective sites of the hard carbon by Li$^+$ ions limiting the breathing mode of sp^2 C atoms in the rings. The decrease of the G band is instead explained by the weakening of resonance caused by intercalation of Li$^+$ ions between graphene planes. At the lower cut-off voltage (i.e. 0.01 V), the intensity of the D and G bands becomes so low that the signals fall within the background generated by the presence of the SEI components on the electrode surface, and cannot be distinguished properly. The progressive decrease of intensity by increasing the lithiation degree is already reported in literature for carbonaceous materials, and it provides confirmation of the mixed adsorption-intercalation mechanism typical of hard carbons [62,68,69]. During de-lithiation, the D and G peaks start increasing again, and can be distinguished even at 0.085 V; however, the intensity ratio between D and G band is slightly lower than the initial one, suggesting a decrease of the D band after Li extraction. This indicates that some defective sites of the carbon matrix remain occupied after the first discharge, contributing to the initial irreversible capacity of the material. However, this partially lithiated state of the hard carbon may act as a Li$^+$ scaffold, increasing the

conductivity of the whole composite and gradually improving the charge transfer kinetics for the subsequent cycles.

In order to further investigate the interfacial properties of the material, impedance spectra were recorded at the bias potential of 0.4 V during the 1st cycle and then every 10th cycle upon lithiation (**Figure 8a-c**), using a three-electrode cell configuration. All the Nyquist plots obtained (**Figure 8b**) are characterized by four main features: (I) an intercept with the real axis in the high frequency region; (II) a small semicircle in the medium frequency region; (III) a bigger semicircle in the medium-to-low frequency region; (IV) a straight line in the low frequency region. The obtained Nyquist plots have been modeled by the Equivalent Circuit method [70], and the related parameters have been calculated through a NLLS fitting protocol by using the RelaxIS3 software (rhd instruments). The intercept (I) at high frequencies represents the migration of Li^+ ions through the electrolyte solution, hence it was modeled as a pure resistive element (R_{el}). The semicircle (II) at medium frequencies is related to the migration of Li^+ ions through the passivation layer with charges accumulating onto its surface, and was modeled as a resistive element (R_{SEI}) in parallel with a capacitor element (C_{SEI}). The bigger semicircle (III) at medium-to-low frequencies can be ascribed to the faradaic charge transfer process with charges accumulating onto the surface of the active material particles, modeled as a resistive element (R_{ct}) in parallel with a capacitor element (C_{dl}). Finally, the line (IV) at low frequency describes a semi-infinite diffusion to a blocking electrode, which was modeled with a Warburg impedance (W) in series with a capacitor element (C_i) indicating intercalation capacitance. The resulting equivalent circuit, written according to Boukamp's notation [71,72], is $R_{el}(R_{SEI}C_{SEI})(R_{ct}C_{dl})WC_i$. For the fitting procedure, the pure capacitive elements were substituted by constant phase elements

(Q), in order to consider the non-ideal, capacitive behavior given by electrode inhomogeneity and surface roughness [70].
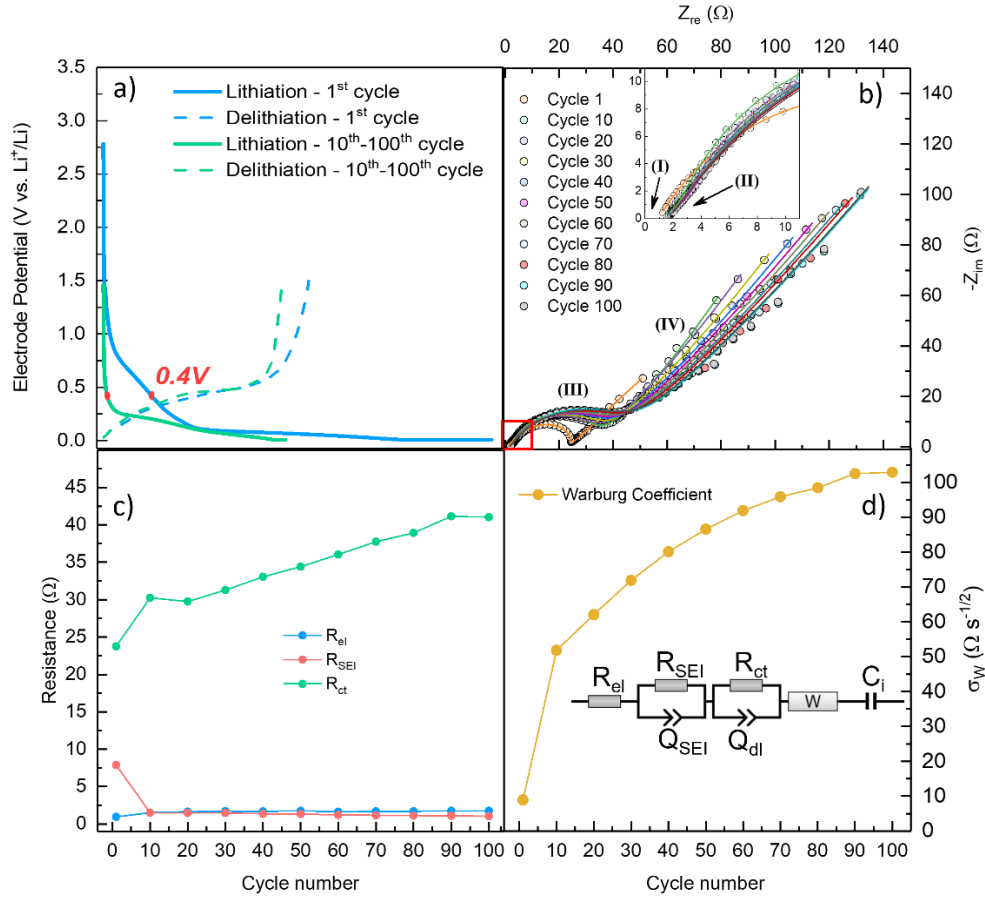

Figure 8. Electrochemical impedance spectroscopy analysis of Si/CCDHC electrode with CS/CA binder: a) Galvanostatic profiles with highlighted acquisition potential during 1st and every 10th cycles; b) Nyquist plots obtained and related fits, with magnification on the high-frequency region (inset); c) Trend of resistances upon cycling; d) Trend of Warburg coefficient upon cycling. The fit results have been obtained by using the equivalent circuit model reported in panel d).

In **Figure 8c-d** the values of R_{el}, R_{SEI}, R_{ct} and σ_W, calculated by using the previously described model for fitting, are reported as a function of the number of cycles, in order to evidence the behavior of the interfaces upon cycling. The resistance of the electrolyte, R_{el}, basically remains constant upon cycling until 100 cycles. The resistance of the passivation layer, R_{SEI}, displays a

higher value in the first cycle due to the formation of the SEI, and then decreases to very low values remaining constant upon cycling. These results suggest the formation of a thin passivation layer during the first discharge, which then remains stable in the subsequent cycles, hence preventing further electrolyte decomposition. This trend is consistent with the results obtained by the galvanostatic cycling in **Figure 3d**, which did not show any obvious charge capacity spikes ascribable to SEI breakage and subsequent reformation. As for the resistance to charge transfer, R_{ct}, a sharp increase is observed from the 1st to the 10th cycle, after which the resistance increment becomes less pronounced; eventually, stabilization is reached between 90 and 100 cycles. The initial sharper increase is consistent with the observations from ex-situ Raman (**Figure 7**), which revealed the presence of insulating Li_2O at the surface of the active material after the first discharge, thus increasing the electrode polarization in the subsequent cycles. Finally, the Warburg coefficient, σ_W, has an increasing trend upon cycling, which translates in progressively more hindered solid-state diffusion of Li^+ and decreasing of diffusion coefficient. However, the sharpest increment is encountered on going from the 1st to the 10th cycle due to the irreversible formation of the passivation layer making the diffusion slower [73]; in the following cycles, the increase bends towards a plateau, indicating a progressive stabilization of diffusion upon cycling.

The interfacial and kinetic properties of the material were also studied within a single cycle at different states of charge, by performing impedance measurements with a sampling interval of 0.02 V upon full lithiation and subsequent de-lithiation during cycle 10, to minimize any bias coming from possible modification of SEI and thickness (**Figure 9a-b**), using a two-electrode cell configuration to avoid inductive contributions at low potentials. For the sake of clarity, only selected diagrams are displayed to give a general trend upon decreasing/increasing potential. A

quite large low-frequency semicircle can be observed at high potentials, which progressively tends to split in two contributions upon lithiation. When charging, the opposite behavior is displayed, with the two semicircles progressively merging into one larger feature. The additional semicircle in the medium-to-low frequency range was attributed to the contribution of the metal Li counter-electrode to the cell impedance, which cannot be approximated to zero in absence of a reference electrode (i.e. in two-electrode configuration here adopted). In order to deconvolute working and counter electrode contributions, the DRT analysis method was applied, by calculating the DRT function γ according to Tikhonov regularization [74]. For the DRT calculation to be valid, the boundary conditions require the convergence of the impedance towards the real axis when ω tends to 0; the typical impedance spectra in LIBs generally do not possess this requirement, as the low-frequency Warburg diffusion diverges from the real axis. For this reason, a pre-processing fit by the Nyquist plot by the equivalent circuit method is required prior to DRT determination [75,76]. Specifically, the raw spectra have been modeled, as a first approximation, according to the equivalent circuit $R_{el}(R_{SEI}C_{SEI})(R_{Li}C_{Li})(R_{ct}C_{dl})WC_i$, taking into account also the contribution from the counter-electrode. For the fitting procedure, the pure capacitive elements were substituted by constant phase element (Q) [71,72]. Then, the low frequency points, as simulated by WC_i elements, were subtracted from the overall impedance.
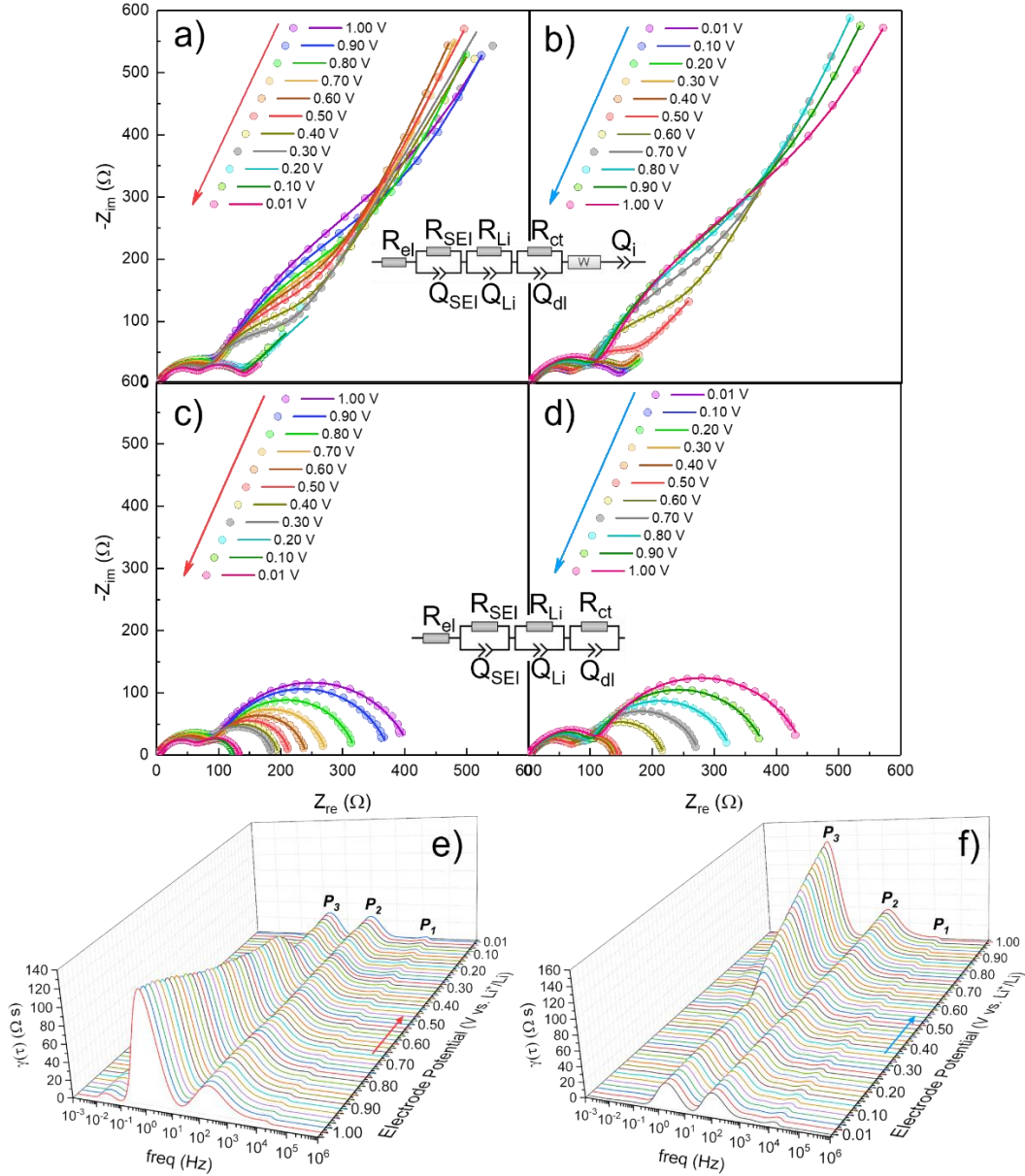
Figure 9. "Staircase" electrochemical impedance spectroscopy analysis of Si/CCDHC electrode with CS/CA binder, performed at the 10th cycle: Nyquist plots obtained during a) lithiation and b) de-lithiation, with related fits and equivalent circuit employed; Nyquist plots after subtraction of the diffusive part displayed for c) lithiation and d) de-lithiation, with related fits and equivalent circuit employed; Distribution of relaxation times for e) lithiation and f) de-lithiation.

The Nyquist plots obtained after subtraction are shown in **Figure 9c-d**. By observing the resulting diagrams, the previously overlapped semicircles are now well split into two

contributions at all potentials. In particular, the medium-to-low frequency semicircle appears to remain almost constant upon discharge and the subsequent charge. The presence of this additional semicircle confirms the contribution of Li counter-electrode to the overall impedance. From the calculation of the DRT (**Figure 9e-f**), the various polarizations, and the associated processes, can be deconvoluted according to their different time constants, resulting in different characteristic frequencies. By calculating the DRT as a function of potential, it was possible to clearly define three main peaks (the small hump at low frequencies is an artifact due to the removal of Warburg diffusion) having different behaviors: P1 is in a high frequency range, consistent with the resistance of the passivation layer (R_{SEI}); P2 remains basically constant and can be related to the contribution of the metal Li counter electrode (R_{Li}); finally, P3 at low frequencies has a strong dependency on the electrode potential, thus suggesting its association with the resistance of charge-transfer (R_{ct}) of the Si/CCDHC electrode. Interestingly, P3 progressively decreases by increasing degree of lithiation, with a sudden drop at about 0.25 V; upon de-lithiation, the opposite behavior is observed, with a sudden increase in peak intensity at about 0.50 V.

Based on the DRT findings, the fits of the impedance dispersions have been repeated on the Nyquist plots obtained after subtraction of the low frequency region (shown in **Figure 9c-d**), by using the equivalent circuit $R_{el}(R_{SEI}C_{SEI})(R_{Li}C_{Li})(R_{ct}C_{dl})$. The calculated values of the circuital elements are reported as a function of electrode potential for the lithiation and de-lithiation processes in **Figure 10a-b**.
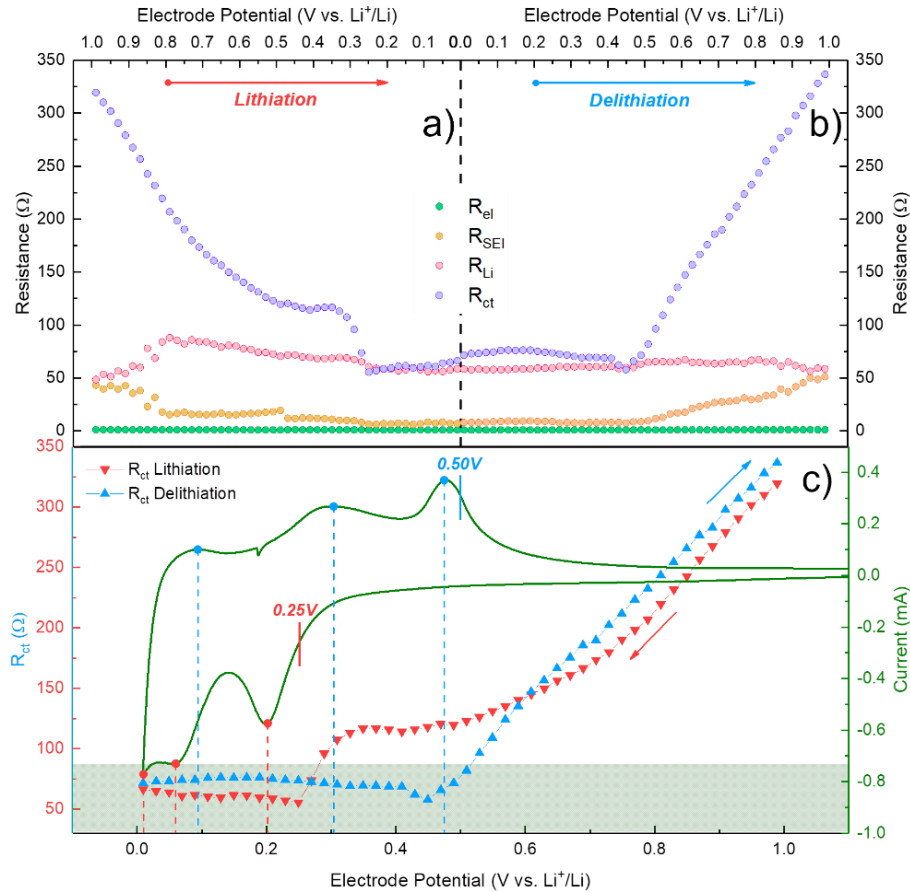
Figure 10. Trend of R_{el}, R_{SEI}, R_{Li} and R_{ct} as a function of potential during a) lithiation and b) de-lithiation; c) Trend of R_{ct} as a function of electrode potential, with correlation to cyclic voltammetry.

The resistance of the electrolyte, R_{el}, always remains constant and very low, as expected. The resistance of the passivation layer, R_{SEI}, displays a higher value at high potential, and progressively decreases when approaching full lithiation; the opposite trend is displayed upon de-lithiation. This result suggests that upon lithiation, the SEI is stretched due to volume expansion of Si particles, becoming thinner but without cracking, thus providing a lower resistance and confirming the observations from ex-situ Raman (**Figure 7**) and from impedance measurements upon cycling (**Figure 8**). The resistance associated to Li metal counter-electrode, R_{Li}, is basically constant throughout the whole cycle, as previously described. As for the resistance associated with charge transfer, R_{ct}, it progressively decreases upon lithiation, and

36

reversibly increases upon de-lithiation. The trend of R_{ct} as a function of potential was correlated to the cyclic voltammetry of the material (**Figure 10c**): the polarization due to charge-transfer reactions drops at 0.25 V upon discharge and sharply increases after 0.50 V upon charge, as observed from **Figure 9e-f**. These values are consistent with the starting and ending of redox activities in the cyclic voltammetry, respectively, and confirm the reversibility of the (de)alloying process within the single cycle.

4. CONCLUSIONS

The performance and stability of a composite anode based on Si and a biomass-derived hard carbon employing a green crosslinked binder were evaluated. The standard galvanostatic cycling displayed quite high performance comparable to those of the same material employing commercial graphite as the buffering matrix, but a higher stability was displayed over prolonged cycling and no SEI breakage is observed. Moreover, the crosslinked binder also proved to be more effective in promoting a higher structural stability with respect to the conventionally studied binders. From the rate capability test, the Si/CCDHC composite showed very high capacity retention and reduced polarization even at high current rates. Ex-situ Raman spectroscopy proved to be a powerful technique in determining the structural stability of the material within the first discharge/charge cycle. The Si was found to undergo irreversible amorphization during the first cycle, and the hard carbon matrix also underwent a partially irreversible lithiation, consistent with the low coulombic efficiency at first cycle. However, the reversibility of the processes was confirmed by impedance spectroscopy measurements performed firstly upon increasing cycle number, and secondly upon full (de)lithiation within a single cycle, aided by the calculation of DRT function. The results showed that the hard carbon matrix is effective in buffering the volume changes upon cycling; moreover, a stable SEI was

formed after the first cycle, providing a limited contribution to the overall impedance and no further electrolyte decomposition in the subsequent cycles. The reversibility of processes was further confirmed by the trend of R_{ct} compared to the redox peaks in cyclic voltammetry, in excellent agreement with the results obtained by ex-situ Raman, impedance measurements and DRT function. Overall, considering the high amount of Si in the formulation, the material displayed promising characteristics as a next-generation anode; moreover, the corn cobs-derived hard carbon was obtained by employing waste biomass as it is, without any treatment prior to pyrolysis, resulting in a more sustainable way of converting wastes to resources. The carbon matrix was indeed able to provide good buffering activity and stability to the system. Therefore, future investigations will be carried out to optimize the electrode formulation and to provide a suitable pre-lithiation technique in order to reduce the irreversible capacity at first cycle, with the aim to test the compatibility in full-cell configuration.

ASSOCIATED CONTENT

Supporting Information

The Supporting Information is available free of charge at _____

Additional Raman spectra, XRD patterns, SEM images, EDX analyses, adopted equations for the bare CCDHC powder; TGA curve of the ball-milled Si/CCDHC composite; cyclic voltammetry and discharge/charge curves of bare CCDHC; discharge/charge curves of bare Si; Raman spectrum on pristine Si/CCDHC electrode with CS/CA binder.

AUTHOR INFORMATION

Corresponding Author

*E-mail: leonardo.sbrascini@unicam.it (L.S.)

ORCID

Leonardo Sbrascini: 0000-0002-2218-7764

Antunes Staffolani: 0000-0002-1144-0074

Luca Bottoni: 0000-0002-4249-4067

Hamideh Darjazi: 0000-0002-3255-3887

Luca Minnetti: 0000-0003-0063-1649

Marco Minicucci: 0000-0001-6459-7000

Francesco Nobili: 0000-0002-0564-2243

Author Contributions

The manuscript was written through contributions of all authors. All authors have given approval to the final version of the manuscript. L.S. and F.N. conceptualized the work and wrote the manuscript. A.S., L.B., H.D. and L.M. contributed to the analysis and discussion. L.S. and M.M. performed and analyzed the Raman measurements. F.N. supervised the work.

Notes

The authors declare no competing financial interest.

REFERENCES

(1)   Diekmann, J.; Hanisch, C.; Froböse, L.; Schälicke, G.; Loellhoeffel, T.; Fölster, A.-S.; Kwade, A. Ecological Recycling of Lithium-Ion Batteries from Electric Vehicles with Focus on Mechanical Processes. *J. Electrochem. Soc.* **2017**, *164* (1), A6184–A6191. https://doi.org/10.1149/2.0271701jes.

(2)   Steward, D.; Mayyas, A.; Mann, M. Economics and Challenges of Li-Ion Battery Recycling from End-of-Life Vehicles. *Procedia Manuf.* **2019**, *33*, 272–279. https://doi.org/10.1016/j.promfg.2019.04.033.

(3)   Xiong, S.; Ji, J.; Ma, X. Environmental and Economic Evaluation of Remanufacturing Lithium-Ion Batteries from Electric Vehicles. *Waste Manag.* **2020**, *102*, 579–586. https://doi.org/10.1016/j.wasman.2019.11.013.

(4)   Xu, C.; Dai, Q.; Gaines, L.; Hu, M.; Tukker, A.; Steubing, B. Future Material Demand for Automotive Lithium-Based Batteries. *Commun. Mater.* **2020**, *1* (1). https://doi.org/10.1038/s43246-020-00095-x.

(5)   Emilsson, E.; Dahllöf, L. *Lithium-Ion Vehicle Battery Production, C444, IVL Swedish Environmental Research Institute*; 2019.

(6)   Larcher, D.; Tarascon, J. M. Towards Greener and More Sustainable Batteries for Electrical Energy Storage. *Nat. Chem.* **2015**, *7* (1), 19–29. https://doi.org/10.1038/nchem.2085.

(7)   Knobloch, F.; Hanssen, S. V.; Lam, A.; Pollitt, H.; Salas, P.; Chewpreecha, U.; Huijbregts, M. A. J.; Mercure, J. F. Net Emission Reductions from Electric Cars and Heat

Pumps in 59 World Regions over Time. *Nat. Sustain.* **2020**, *3* (6), 437–447. https://doi.org/10.1038/s41893-020-0488-7.

(8)   Hannan, M. A.; Hoque, M. M.; Hussain, A.; Yusof, Y.; Ker, P. J. State-of-the-Art and Energy Management System of Lithium-Ion Batteries in Electric Vehicle Applications: Issues and Recommendations. *IEEE Access* **2018**, *6*, 19362–19378. https://doi.org/10.1109/ACCESS.2018.2817655.

(9)   Andre, D.; Kim, S. J.; Lamp, P.; Lux, S. F.; Maglia, F.; Paschos, O.; Stiaszny, B. Future Generations of Cathode Materials: An Automotive Industry Perspective. *J. Mater. Chem. A* **2015**, *3* (13), 6709–6732. https://doi.org/10.1039/c5ta00361j.

(10)   Iqbal, A.; Chen, L.; Chen, Y.; Gao, Y.; Chen, F.; Li, D. Lithium-Ion Full Cell with High Energy Density Using Nickel-Rich $LiNi_{0.8}Co_{0.1}Mn_{0.1}O_2$ Cathode and SiO-C Composite Anode. *Int. J. Miner. Metall. Mater.* **2018**, *25* (12), 1473–1474.

(11)   Gaines, L.; Richa, K.; Spangenberger, J. Key Issues for Li-Ion Battery Recycling. *MRS Energy Sustain.* **2018**, *5* (1), 1–14. https://doi.org/10.1557/mre.2018.13.

(12)   Mossali, E.; Picone, N.; Gentilini, L.; Rodrìguez, O.; Pérez, J. M.; Colledani, M. Lithium-Ion Batteries towards Circular Economy: A Literature Review of Opportunities and Issues of Recycling Treatments. *J. Environ. Manage.* **2020**, *264*. https://doi.org/10.1016/j.jenvman.2020.110500.

(13)   Wang, J.; Nie, P.; Ding, B.; Dong, S.; Hao, X.; Dou, H.; Zhang, X. Biomass Derived Carbon for Energy Storage Devices. *J. Mater. Chem. A* **2017**, *5* (6), 2411–2428. https://doi.org/10.1039/c6ta08742f.

(14)   Zhang, W. J. A Review of the Electrochemical Performance of Alloy Anodes for Lithium-Ion Batteries. *J. Power Sources* **2011**, *196* (1), 13–24. https://doi.org/10.1016/j.jpowsour.2010.07.020.

(15)   Franco Gonzalez, A.; Yang, N.-H.; Liu, R.-S. Silicon Anode Design for Lithium-Ion Batteries: Progress and Perspectives. *J. Phys. Chem. C* **2017**, *121* (50), 27775–27787. https://doi.org/10.1021/acs.jpcc.7b07793.

(16)   Shen, X.; Zhang, X.-Q.; Ding, F.; Huang, J.-Q.; Xu, R.; Chen, X.; Yan, C.; Su, F.-Y.; Chen, C.-M.; Liu, X.; Zhang, Q. Advanced Electrode Materials in Lithium Batteries: Retrospect and Prospect. *Energy Mater. Adv.* **2021**, *2021*, 1–15. https://doi.org/10.34133/2021/1205324.

(17)   Lu, J.; Chen, Z.; Pan, F.; Cui, Y.; Amine, K. High-Performance Anode Materials for Rechargeable Lithium-Ion Batteries. *Electrochem. Energy Rev.* **2018**, *1* (1), 35–53. https://doi.org/10.1007/s41918-018-0001-4.

(18)   Li, J. Y.; Xu, Q.; Li, G.; Yin, Y. X.; Wan, L. J.; Guo, Y. G. Research Progress Regarding Si-Based Anode Materials towards Practical Application in High Energy Density Li-Ion Batteries. *Mater. Chem. Front.* **2017**, *1* (9), 1691–1708. https://doi.org/10.1039/c6qm00302h.

(19)   Ji, L.; Lin, Z.; Alcoutlabi, M.; Zhang, X. Recent Developments in Nanostructured Anode Materials for Rechargeable Lithium-Ion Batteries. *Energy Environ. Sci.* **2011**, *4* (8), 2682–2689. https://doi.org/10.1039/c0ee00699h.

(20)   Zhou, X.; Yin, Y.; Wan, L.; Guo, Y. Self-Assembled Nanocomposite of Silicon

Nanoparticles Encapsulated in Graphene through Electrostatic Attraction for Lithium-Ion Batteries. https://doi.org/10.1002/aenm.201200158.

(21) Zhou, X.; Wan, L.; Guo, Y. Binding SnO_2 Nanocrystals in Nitrogen-Doped Graphene Sheets as Anode Materials for Lithium-Ion Batteries. https://doi.org/10.1002/adma.201300071.

(22) Dou, F.; Shi, L.; Chen, G.; Zhang, D. *Silicon/Carbon Composite Anode Materials for Lithium-Ion Batteries*; Springer Singapore, 2019; Vol. 2. https://doi.org/10.1007/s41918-018-00028-w.

(23) Wang, J.; Zhao, H.; Liu, X.; Wang, J.; Wang, C. Electrochemical Properties of SnO_2/Carbon Composite Materials as Anode Material for Lithium-Ion Batteries. *Electrochim. Acta* **2011**, *56* (18), 6441–6447. https://doi.org/10.1016/j.electacta.2011.04.134.

(24) Baldinelli, A.; Dou, X.; Buchholz, D.; Marinaro, M.; Passerini, S.; Barelli, L. Addressing the Energy Sustainability of Biowaste-Derived Hard Carbon Materials for Battery Electrodes. *Green Chem.* **2018**, *20* (7), 1527–1537. https://doi.org/10.1039/c8gc00085a.

(25) Erk, C.; Brezesinski, T.; Sommer, H.; Schneider, R.; Janek, J. Toward Silicon Anodes for Next-Generation Lithium Ion Batteries: A Comparative Performance Study of Various Polymer Binders and Silicon Nanopowders. *ACS Appl. Mater. Interfaces* **2013**, *5* (15), 7299–7307. https://doi.org/10.1021/am401642c.

(26) Hu, S.; Cai, Z.; Huang, T.; Zhang, H.; Yu, A. A Modified Natural Polysaccharide as a High-Performance Binder for Silicon Anodes in Lithium-Ion Batteries. *ACS Appl. Mater.*

Interfaces **2019**, *11* (4), 4311–4317. https://doi.org/10.1021/acsami.8b15695.

(27)   Kuenzel, M.; Porhiel, R.; Bresser, D.; Asenbauer, J.; Axmann, P.; Wohlfahrt-Mehrens, M.; Passerini, S. Deriving Structure-Performance Relations of Chemically Modified Chitosan Binders for Sustainable High-Voltage $LiNi_{0.5}Mn_{1.5}O_4$ Cathodes . *Batter. Supercaps* **2020**, *3* (2), 155–164. https://doi.org/10.1002/batt.201900140.

(28)   Shen, L.; Shen, L.; Wang, Z.; Chen, L. In Situ Thermally Cross-Linked Polyacrylonitrile as Binder for High-Performance Silicon as Lithium Ion Battery Anode. *ChemSusChem* **2014**, *7* (7), 1951–1956. https://doi.org/10.1002/cssc.201400030.

(29)   Espinosa-Villatoro, E.; Nelson Weker, J.; Ko, J. S.; Quiroga-González, E. Tracking the Evolution of Processes Occurring in Silicon Anodes in Lithium Ion Batteries by 3D Visualization of Relaxation Times. *J. Electroanal. Chem.* **2021**, *892* (March), 115309. https://doi.org/10.1016/j.jelechem.2021.115309.

(30)   Guo, J.; Sun, A.; Chen, X.; Wang, C.; Manivannan, A. Cyclability Study of Silicon-Carbon Composite Anodes for Lithium-Ion Batteries Using Electrochemical Impedance Spectroscopy. *Electrochim. Acta* **2011**, *56* (11), 3981–3987. https://doi.org/10.1016/j.electacta.2011.02.014.

(31)   Ciucci, F.; Chen, C. Analysis of Electrochemical Impedance Spectroscopy Data Using the Distribution of Relaxation Times: A Bayesian and Hierarchical Bayesian Approach. *Electrochim. Acta* **2015**, *167*, 439–454. https://doi.org/10.1016/j.electacta.2015.03.123.

(32)   Venkateswara Rao, C.; Soler, J.; Katiyar, R.; Shojan, J.; West, W. C.; Katiyar, R. S. Investigations on Electrochemical Behavior and Structural Stability of

$Li_{1.2}Mn_{0.54}Ni_{0.13}Co_{0.13}O_2$ Lithium-Ion Cathodes via in-Situ and Ex-Situ Raman Spectroscopy. *J. Phys. Chem. C* **2014**, *118* (26), 14133–14141. https://doi.org/10.1021/jp501777v.

(33) Zhang, C.; Wang, F.; Han, J.; Bai, S.; Tan, J.; Liu, J.; Li, F. Challenges and Recent Progress on Silicon-Based Anode Materials for Next-Generation Lithium-Ion Batteries. *Small Struct.* **2021**, *2* (6), 2100009. https://doi.org/10.1002/sstr.202100009.

(34) Moyassari, E.; Streck, L.; Paul, N.; Trunk, M.; Neagu, R.; Chang, C.-C.; Hou, S.-C.; Märkisch, B.; Gilles, R.; Jossen, A. Impact of Silicon Content within Silicon-Graphite Anodes on Performance and Li Concentration Profiles of Li-Ion Cells Using Neutron Depth Profiling. *J. Electrochem. Soc.* **2021**, *168* (2), 020519. https://doi.org/10.1149/1945-7111/abe1db.

(35) Ferrari, A. C.; Robertson, J. Interpretation of Raman Spectra of Disordered and Amorphous Carbon. *Phys. Rev. B* **2000**, *61* (20). https://doi.org/10.1007/BF02543692.

(36) Darjazi, H.; Staffolani, A.; Sbrascini, L.; Bottoni, L.; Tossici, R.; Nobili, F. Sustainable Anodes for Lithium- and Sodium-Ion Batteries Based on Coffee Ground-Derived Hard Carbon and Green Binders. *Energies* **2020**, *13* (23), 6216. https://doi.org/10.3390/en13236216.

(37) Beda, A.; Taberna, P. L.; Simon, P.; Matei Ghimbeu, C. Hard Carbons Derived from Green Phenolic Resins for Na-Ion Batteries. *Carbon N. Y.* **2018**, *139*, 248–257. https://doi.org/10.1016/j.carbon.2018.06.036.

(38) Velez, V.; Ramos-Sánchez, G.; Lopez, B.; Lartundo-Rojas, L.; González, I.; Sierra, L.

Synthesis of Novel Hard Mesoporous Carbons and Their Application as Anodes for Li and Na Ion Batteries. *Carbon N. Y.* **2019**, *147*, 214–226. https://doi.org/10.1016/j.carbon.2019.02.083.

(39) Spizzirri, P. G.; Fang, J. H.; Rubanov, S.; Gauja, E.; Prawer, S. Nano-Raman Spectroscopy of Silicon Surfaces. *Mater. Forum* **2008**, *34*, 161–166.

(40) Zwick, A.; Carles, R. Multiple-Order Raman Scattering in Crystalline and Amorphous Silicon. *Phys. Rev. B* **1993**, *48* (9), 6024–6032. https://doi.org/10.1103/PhysRevB.48.6024.

(41) Mishra, P.; Jain, K. P. First- and Second-Order Raman Scattering in Nanocrystalline Silicon. *Phys. Rev. B - Condens. Matter Mater. Phys.* **2001**, *64* (7), 733041–733044. https://doi.org/10.1103/PhysRevB.64.073304.

(42) Kravets, V. G.; Kolmykova, V. Y. Raman Scattering of Light in Silicon Nanostructures: First- and Second-Order Spectra. *Opt. Spectrosc. (English Transl. Opt. i Spektrosk.* **2005**, *99* (1), 68–73. https://doi.org/10.1134/1.1999895.

(43) Newbury, D. E.; Ritchie, N. W. M. Is Scanning Electron Microscopy/Energy Dispersive X-Ray Spectrometry (SEM/EDS) Quantitative? *Scanning* **2013**, *35* (3), 141–168. https://doi.org/10.1002/sca.21041.

(44) Wu, J. J.; Bennett, W. R. Fundamental Investigation of Si Anode in Li-Ion Cells. *2012 IEEE Energytech, Energytech 2012* **2012**, 1–5. https://doi.org/10.1109/EnergyTech.2012.6304667.

(45) Maroni, F.; Carbonari, G.; Croce, F.; Tossici, R.; Nobili, F. Anatase TiO_2 as a Cheap and Sustainable Buffering Filler for Silicon Nanoparticles in Lithium-Ion Battery Anodes. *ChemSusChem* **2017**, *10* (23), 4771–4777. https://doi.org/10.1002/cssc.201701431.

(46) Yu, X.; Xue, F.; Huang, H.; Liu, C.; Yu, J.; Sun, Y.; Dong, X.; Cao, G.; Jung, Y. Synthesis and Electrochemical Properties of Silicon Nanosheets by DC Arc Discharge for Lithium-Ion Batteries. *Nanoscale* **2014**, *6* (12), 6860–6865. https://doi.org/10.1039/c3nr06418b.

(47) Kang, K.; Lee, H. S.; Han, D. W.; Kim, G. S.; Lee, D.; Lee, G.; Kang, Y. M.; Jo, M. H. Maximum Li Storage in Si Nanowires for the High Capacity Three-Dimensional Li-Ion Battery. *Appl. Phys. Lett.* **2010**, *96* (5). https://doi.org/10.1063/1.3299006.

(48) Levi, M. D.; Aurbach, D. The Mechanism of Lithium Intercalation in Graphite Film Electrodes in Aprotic Media. Part 1. High Resolution Slow Scan Rate Cyclic Voltammetric Studies and Modeling. *J. Electroanal. Chem.* **1997**, *421* (1–2), 79–88. https://doi.org/10.1016/S0022-0728(96)04832-2.

(49) Wang, N.; Liu, Q.; Sun, B.; Gu, J.; Yu, B.; Zhang, W.; Zhang, D. N-Doped Catalytic Graphitized Hard Carbon for High-Performance Lithium/Sodium-Ion Batteries. *Sci. Rep.* **2018**, *8* (1), 1–8. https://doi.org/10.1038/s41598-018-28310-3.

(50) Saha, P.; Mohanta, T. R.; Kumar, A. SEI Layer and Impact on Si-Anodes for Li-Ion Batteries. *Silicon Anode Syst. Lithium-Ion Batter.* **2022**, 183–263. https://doi.org/10.1016/B978-0-12-819660-1.00001-3.

(51) Shen, C.; Fang, X.; Ge, M.; Zhang, A.; Liu, Y.; Ma, Y.; Mecklenburg, M.; Nie, X.; Zhou,

C. Hierarchical Carbon-Coated Ball-Milled Silicon: Synthesis and Applications in Free-Standing Electrodes and High-Voltage Full Lithium-Ion Batteries. *ACS Nano* **2018**, *12* (6), 6280–6291. https://doi.org/10.1021/acsnano.8b03312.

(52)   Cheng, X. W.; Zhao, D. L.; Wu, L. L.; Ding, Z. W.; Hu, T.; Meng, S. Core-Shell Structured Si@Ni Nanoparticles Encapsulated in Graphene Nanosheet for Lithium Ion Battery Anodes with Enhanced Reversible Capacity and Cyclic Performance. *Electrochim. Acta* **2018**, *265*, 348–354. https://doi.org/10.1016/j.electacta.2018.01.198.

(53)   Nzabahimana, J.; Guo, S.; Hu, X. Facile Synthesis of Si@void@C Nanocomposites from Low-Cost Microsized Si as Anode Materials for Lithium-Ion Batteries. *Appl. Surf. Sci.* **2019**, *479*, 287–295. https://doi.org/10.1016/j.apsusc.2019.01.215.

(54)   Fan, P.; Mu, T.; Lou, S.; Cheng, X.; Gao, Y.; Du, C.; Zuo, P.; Ma, Y.; Yin, G. Amorphous Carbon-Encapsulated Si Nanoparticles Loading on MCMB with Sandwich Structure for Lithium Ion Batteries. *Electrochim. Acta* **2019**, *306*, 590–598. https://doi.org/10.1016/j.electacta.2019.03.154.

(55)   Wang, Z.; Zheng, B.; Liu, H.; Zhang, C.; Wu, F.; Luo, H.; Yu, P. One-Step Synthesis of Nanoporous Silicon @ Graphitized Carbon Composite and Its Superior Lithium Storage Properties. *J. Alloys Compd.* **2021**, *861*, 157955. https://doi.org/10.1016/j.jallcom.2020.157955.

(56)   Yu, C.; Tian, X.; Xiong, Z.; Zhang, Z.; Sun, Z.; Piao, X. High Stability of Sub-Micro-Sized Silicon/Carbon Composites Using Recycling Silicon Waste for Lithium-Ion Battery Anode. *J. Alloys Compd.* **2021**, *869*, 159124.

https://doi.org/10.1016/j.jallcom.2021.159124.

(57)   Liu, W.; Wang, J.; Wang, J.; Guo, X.; Yang, H. Three-Dimensional Nitrogen-Doped Carbon Coated Hierarchically Porous Silicon Composite as Lithium-Ion Battery Anode. *J. Alloys Compd.* **2021**, *874*, 159921. https://doi.org/10.1016/j.jallcom.2021.159921.

(58)   Liu, Z.; Du, J.; Jia, H.; Wang, W.; Zhang, M.; Ma, J.; Nie, Y.; Liu, T.; Song, K. Design of Hierarchical Buffer Structure for Silicon/Carbon Composite as a High-Performance Li-Ion Batteries Anode. *J. Mater. Sci. Mater. Electron.* **2022**, *33* (6), 3002–3015. https://doi.org/10.1007/s10854-021-07500-2.

(59)   Qi, C.; Li, S.; Yang, Z.; Xiao, Z.; Zhao, L.; Yang, F.; Ning, G.; Ma, X.; Wang, C.; Xu, J.; Gao, J. Suitable Thickness of Carbon Coating Layers for Silicon Anode. *Carbon N. Y.* **2022**, *186*, 530–538. https://doi.org/10.1016/j.carbon.2021.10.062.

(60)   Zhao, J.; Rui, B.; Wei, W.; Nie, P.; Chang, L.; Xue, X.; Wang, L.; Jiang, J. Encapsulating Silicon Particles by Graphitic Carbon Enables High-Performance Lithium-Ion Batteries. *J. Colloid Interface Sci.* **2022**, *607*, 1562–1570. https://doi.org/10.1016/j.jcis.2021.09.005.

(61)   Nanda, J.; Datta, M. K.; Remillard, J. T.; O'Neill, A.; Kumta, P. N. In Situ Raman Microscopy during Discharge of a High Capacity Silicon-Carbon Composite Li-Ion Battery Negative Electrode. *Electrochem. commun.* **2009**, *11* (1), 235–237. https://doi.org/10.1016/j.elecom.2008.11.006.

(62)   Krause, A.; Tkacheva, O.; Omar, A.; Langklotz, U.; Giebeler, L.; Dörfler, S.; Fauth, F.; Mikolajick, T.; Weber, W. M. In Situ Raman Spectroscopy on Silicon Nanowire Anodes Integrated in Lithium Ion Batteries. *J. Electrochem. Soc.* **2019**, *166* (3), A5378–A5385.

https://doi.org/10.1149/2.0541903jes.

(63)   Sifuentes, A.; Stowe, A. C.; Smyrl, N. Determination of the Role of Li_2O on the Corrosion of Lithium Hydride. *J. Alloys Compd.* **2013**, *580* (SUPPL1), S271–S273. https://doi.org/10.1016/j.jallcom.2013.02.046.

(64)   Zając, A.; Hanuza, J.; Wandas, M.; Dymińska, L. Determination of N-Acetylation Degree in Chitosan Using Raman Spectroscopy. *Spectrochim. Acta - Part A Mol. Biomol. Spectrosc.* **2015**, *134*, 114–120. https://doi.org/10.1016/j.saa.2014.06.071.

(65)   Hy, S.; Felix; Chen, Y. H.; Liu, J. Y.; Rick, J.; Hwang, B. J. In Situ Surface Enhanced Raman Spectroscopic Studies of Solid Electrolyte Interphase Formation in Lithium Ion Battery Electrodes. *J. Power Sources* **2014**, *256*, 324–328. https://doi.org/10.1016/j.jpowsour.2014.01.092.

(66)   Domi, Y.; Doi, T.; Nakagawa, H.; Yamanaka, T.; Abe, T.; Ogumi, Z. In Situ Raman Study on Reversible Structural Changes of Graphite Negative-Electrodes at High Potentials in $LiPF_6$-Based Electrolyte Solution . *J. Electrochem. Soc.* **2016**, *163* (10), A2435–A2440. https://doi.org/10.1149/2.1301610jes.

(67)   Sole, C.; Drewett, N. E.; Hardwick, L. J. In Situ Raman Study of Lithium-Ion Intercalation into Microcrystalline Graphite. *Faraday Discuss.* **2014**, *172*, 223–237. https://doi.org/10.1039/c4fd00079j.

(68)   Cheng, X. Q.; Li, H. J.; Zhao, Z. X.; Wang, Y. Z.; Wang, X. M. The Use of In-Situ Raman Spectroscopy in Investigating Carbon Materials as Anodes of Alkali Metal-Ion Batteries. *Xinxing Tan Cailiao/New Carbon Mater.* **2021**, *36* (1), 93–105.

https://doi.org/10.1016/S1872-5805(21)60007-0.

(69) Huang, S.; Li, Z.; Wang, B.; Zhang, J.; Peng, Z.; Qi, R.; Wang, J.; Zhao, Y. N-Doping and Defective Nanographitic Domain Coupled Hard Carbon Nanoshells for High Performance Lithium/Sodium Storage. *Adv. Funct. Mater.* **2018**, *28* (10), 1–10. https://doi.org/10.1002/adfm.201706294.

(70) Barsoukov, E.; Macdonald, J. R. *Impedance Spectroscopy - Theory, Experiment and Applications*; 2005.

(71) Boukamp, B. A. A Nonlinear Least Squares Fit Procedure for Analysis of Immittance Data of Electrochemical Systems. *Solid State Ionics* **1986**, *20*, 31–44.

(72) Boukamp, B. A. A Package for Impedance/Admittance Data Analysis. *Solid State Ionics* **1986**, *18–19* (PART 1), 136–140. https://doi.org/10.1016/0167-2738(86)90100-1.

(73) Tröltzsch, U.; Kanoun, O.; Tränkler, H. R. Characterizing Aging Effects of Lithium Ion Batteries by Impedance Spectroscopy. *Electrochim. Acta* **2006**, *51* (8–9), 1664–1672. https://doi.org/10.1016/j.electacta.2005.02.148.

(74) Gavrilyuk, A. L.; Osinkin, D. A.; Bronin, D. I. The Use of Tikhonov Regularization Method for Calculating the Distribution Function of Relaxation Times in Impedance Spectroscopy. *Russ. J. Electrochem.* **2017**, *53* (6), 575–588. https://doi.org/10.1134/S1023193517060040.

(75) Illig, J.; Ender, M.; Chrobak, T.; Schmidt, J. P.; Klotz, D.; Ivers-Tiffée, E. Separation of Charge Transfer and Contact Resistance in $LiFePO_4$-Cathodes by Impedance Modeling .

J. Electrochem. Soc. **2012**, *159* (7), A952–A960. https://doi.org/10.1149/2.030207jes.

(76)   Pan, K.; Zou, F.; Canova, M.; Zhu, Y.; Kim, J. H. Comprehensive Electrochemical Impedance Spectroscopy Study of Si-Based Anodes Using Distribution of Relaxation Times Analysis. *J. Power Sources* **2020**, *479* (June), 229083. https://doi.org/10.1016/j.jpowsour.2020.229083.